Accepted Manuscript

Buckling and postbuckling of biaxially compressed functionally graded multilayer graphene nanoplatelet-reinforced polymer composite plates

Mitao Song , Jie Yang , Sritawat Kitipornchai , Weidong Zhu

Please cite this article as: Mitao Song , Jie Yang , Sritawat Kitipornchai , Weidong Zhu , Buckling and postbuckling of biaxially compressed functionally graded multilayer graphene nanoplatelet-reinforced polymer composite plates, *International Journal of Mechanical Sciences* (2017), doi: 10.1016/j.ijmecsci.2017.07.017

This is a PDF file of an unedited manuscript that has been accepted for publication. As a service to our customers we are providing this early version of the manuscript. The manuscript will undergo copyediting, typesetting, and review of the resulting proof before it is published in its final form. Please note that during the production process errors may be discovered which could affect the content, and all legal disclaimers that apply to the journal pertain.

Highlights

- Buckling and postbuckling of biaxially compressed functionally graded multilayer GPLRC plates are investigated.

- The material properties of the GPL-reinforced composite (GPLRC) are evaluated through a micromechanics model.

- Theoretical formulations based on the first-order shear deformation plate theory and von Kármán-type nonlinear kinematics are developed.

- A two step perturbation technique is employed to determine the asymptotic postbuckling solutions of both perfect and imperfect plates.

- The effects of GPL weight fraction, distribution pattern, geometry on buckling and postbuckling behaviors of GPLRC plates are examined.

Buckling and postbuckling of biaxially compressed functionally graded multilayer graphene nanoplatelet-reinforced polymer composite plates

Mitao Song [a, b], Jie Yang [c,*], Sritawat Kitipornchai [a], Weidong Zhu [d]

[a] School of Civil Engineering, The University of Queensland, St Lucia, Brisbane, QLD 4072 Australia

[b] Faculty of Civil Engineering and Mechanics, Jiangsu University, Zhenjiang, Jiangsu, 212013 P.R. China

[c] School of Engineering, RMIT University, PO Box 71, Bundoora, VIC 3083 Australia

[d] Department of Mechanical Engineering, University of Maryland, Baltimore County, Baltimore, MD 21250, USA

ABSTRACT

The present paper investigates the biaxially compressed buckling and postbuckling behaviors of functionally graded multilayer composite plates reinforced with a low content of graphene nanoplatelets (GPLs) that are randomly oriented and uniformly dispersed in the polymer matrix within each individual layer. The material properties of the GPL-reinforced composite (GPLRC), which are graded along the thickness direction due to a layer-wise change in GPL weight fraction, are evaluated through a micromechanics model. Theoretical formulations are based on the first-order shear deformation plate theory and von Kármán-type nonlinear kinematics and include the effect of an initial geometric imperfection. A two step perturbation technique is employed to determine the asymptotic postbuckling solutions and the biaxial compressive postbuckling equilibrium paths of both perfect and

imperfect plates simply supported on all edges. The effects of GPL weight fraction, distribution pattern, geometry and size as well as total number of layers on the buckling and postbuckling behaviors of functionally graded GPLRC plates are examined in detail.

---

[*] Corresponding author. Tel.: 61-03-99256169; Fax: 61-03-99256108

E-mail address: j.yang@rmit.edu.au (J. Yang)

1. Introduction

Functionally graded materials (FGMs) are advanced inhomogeneous composites characterized by a continuously varying material composition and properties in one or more dimensions of the structure to achieve desired performance goals. Due to the elimination of distinct interfaces between different materials, mechanical stress concentration can be significantly alleviated and mechanical properties can be spatially controlled [1-3]. Owing to the unique advantages it offers over the traditional homogeneous composites, the concept of FGMs has been applied to a wide range of engineering applications in mechanical, electronic, optical, chemical, biomechanical, civil, aerospace, nuclear, automotive, and shipbuilding industries [4].

Due to the exceptional mechanical, thermal and electrical properties of carbon nanotubes (CNTs), polymer nanocomposites reinforced with CNTs have attracted huge attention from research and industry communities [5]. Shen [6] found that the mechanical properties of the polymer/CNTs nanocomposites can be further improved when CNTs are nonuniformly distributed in the polymer matrix. The structural analyses of functionally graded polymer/CNTs nanocomposites, such as the static bending, elastic buckling, postbuckling, free and forced vibrations, have recently been extensively investigated [6-15]. Compared with CNTs, graphene and graphene nanoplatelets (GPLs) [16] have much bigger specific surface areas which provide much stronger bonding with the matrix hence the greatly enhanced load transfer capability. Rafiee et al. [17] reported that by adding 0.1% weight fraction (wt.%) of GPLs, the strength and stiffness of the reinforced epoxy nanocomposites are enhanced by the same degree achieved by adding 1.0 wt.% of CNTs. Besides, graphene and its derivatives are abundant in nature and have a lower manufacturing cost when compared with CNTs. These merits make graphene and GPLs outstanding candidates as the reinforcement materials to improve the mechanical properties of polymeric materials. So far, the marjority of the research efforts in this emerging area have been directed towards the synthesis/fabrication techniques and material property characterization of the polymer/graphene nanocomposites. Fang et al. [18] manufactured polystyrene/graphene nanocomposites by dispersing graphene sheets in polystyrene, and found that an addition of 0.9 wt.% graphene sheets results in a 70% increase in tensile strength and a 57% increase in Young's modulus.

4

Zhao et al. [19] dispersed 1.8 wt.% of graphene oxide in poly (vinyl alcohol) (PVA) matrix and reduced the dispersed graphene oxide into graphene sheets. They found that the Young's modulus of graphene-reinforced PVA composite films increases almost 10 times. Wang et al. [20] added GPLs with different sizes into epoxy matrix using a sonication process followed by three-roll milling. Their study showed that the use of GPLs with a larger size can lead to new nanocomposites with a considerably increased tensile modulus. Ji et al. [21] performed numerical simulations by using Mori-Tanaka micromechanics method to investigate the effective elastic properties of graphene-reinforced polymeric nanocomposites, and verified that graphene sheets dramatically outperform CNTs as reinforcement nanofillers. Rahman and Haque [22] studied the mechanical properties of graphene/epoxy nanocomposites using molecular dynamics simulations, and observed that dispersing graphene with a high aspect ratio provides improved in-plane Young's modulus of graphene/epoxy nanocomposites in comparison to agglomerated graphene system. Montazeri and Rafii-Tabar [23] employed a multiscale modeling approach to analyze the mechanical properties of graphene-reinforced polymeric nanocomposites. Their results discovered that the presence of ripples on the surface of the embedded graphene sheets can decrease the axial Young modulus of the nanocomposites.

In spite of its practical importance, researches on the structural behavior of graphene-reinforced composites is very limited. Among those, Chandra et al. [24] proposed a multiscale finite element method for the free vibration of graphene/polymer composites by modeling graphene and polymer matrix with the atomistic and conventional continuum finite element methods, respectively. Cranford [25] used a hybrid atomistic and molecular dynamics approach to study the buckling induced delamination of mono- and bilayer graphene-based composites. Rissanou et al. [26] presented the structural and dynamic analyses of several graphene-based polymer nanocomposites with graphene sheets of different sizes through atomistic molecular dynamic simulations. It should be noted that previous studies were focused on the nanocomposites reinforced graphene layers uniformly dispersed in the matrix only. Most recently, Yang and his co-workers [27] introduced the concept of FGMs to graphene reinforced polymer nanocomposites in which GPLs are non-uniformly dispersed in the epoxy matrix and investigated the free and forced vibrations [27], nonlinear bending [28], buckling and

5

postbuckling [29], dynamic stability [30], large amplitude vibration [31, 32] of functionally graded multilayer GPL-reinforced composite (GPLRC) beams and plates. They found that an appropriately chosen GPL distribution pattern can offer much better reinforcing effect than the uniform distribution. By employing higher-order shear deformation plate theory, Shen et al. [33, 34] studied the nonlinear bending and nonlinear vibration of functionally graded composite laminated plates reinforced with graphene sheets under a uniform temperature field. To the best of the authors' knowledge, there is still no previous study on the buckling and postbuckling analysis of biaxially compressed functionally graded multilayer GPLRC plates.

For the structural analysis of composite plates, recently several effective and accurate plate theories have been developed, such as third-order shear deformation plate theories [35-37], a simple first-order shear deformation plate theory [38], and a Quasi-3D hyperbolic shear deformation theory [39]. At the same time, efforts also focused on the development of effective solution methods, such as the meshfree methods [10-12, 40-42], the variational differential quadrature method [43], the isogeometric analysis methods [44-46], and the perturbation method [47]. Compared to the perturbation method, the numerical methods have proven their efficiency to solve a more larger number of engineering problems, especially the mesh-free methods, which can deal with large deformation problems and crack propagarion problems. However, the asympototic approach has its own advantages, by providing a good physical insight into the problem considered, and easily assessing the influence of all the parameters on the solution.

Within the framework of the first-order shear deformation theory (FSDT) to incorporate the effect of transverse shear strain and von Kármán nonlinear kinematics to take into account the geometically nonlinear deformation, this paper investigates the buckling and postbuckling behaviors of functionally graded multilayer GPLRC plates under bixial compression. The micromechanics based Halpin-Tsai model is employed to predict the effective Young's modulus of the nanocomposite while the rule of mixture is used to determine its effective Poisson's ratio. A two step perturbation technique is used to trace the postbuckling equilibrium paths of functionally graded multilayer GPLRC plates with all edges simply supported. After the validation studies with comparisons between the results obtained by the present

6

formulation and those by experiments and a higher-order shear deformation plate theory (HSDPT) in the existing literatures, a comprehensive parametric study is conducted to highlight the effects of GPL distribution pattern, weight fraction, geometry and size as well as the total number of layers on the buckling and postbuckling behaviors of the GPLRC plates.

2. Problem Formulation

A rectangular laminated composite plate of length a, width b and total thickness h that is composed of a total of N perfectly bonded GPL/polymer nanocomposite layers with equal thickness h/N is shown in Fig. 1. The plate is subjected to uniformly distributed biaxial compression N_x and N_y along the edges $x = 0, a$ and $y = 0, b$, respectively. GPL nanofillers are randomly oriented and uniformly dispersed in the polymer matrix within each individual layer. 4 different GPL distributions, including uniform (UD) and functionally graded (FG-O, FG-X) as shown in Fig. 2, are considered in the analysis. In FG distributions, the GPL weight fraction varies linearly from layer to layer along the thickness direction so that it is maximum at the mid-plance of the FG-O plate but at both the top and bottom surfaces of the FG-X plate.
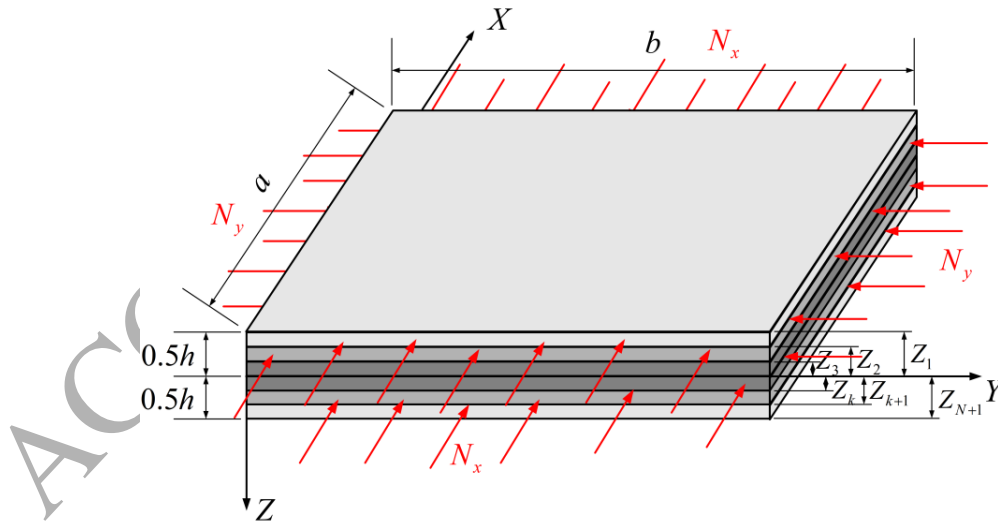

Fig. 1. A functionally graded multilayer GPLRC plate under bixial compression
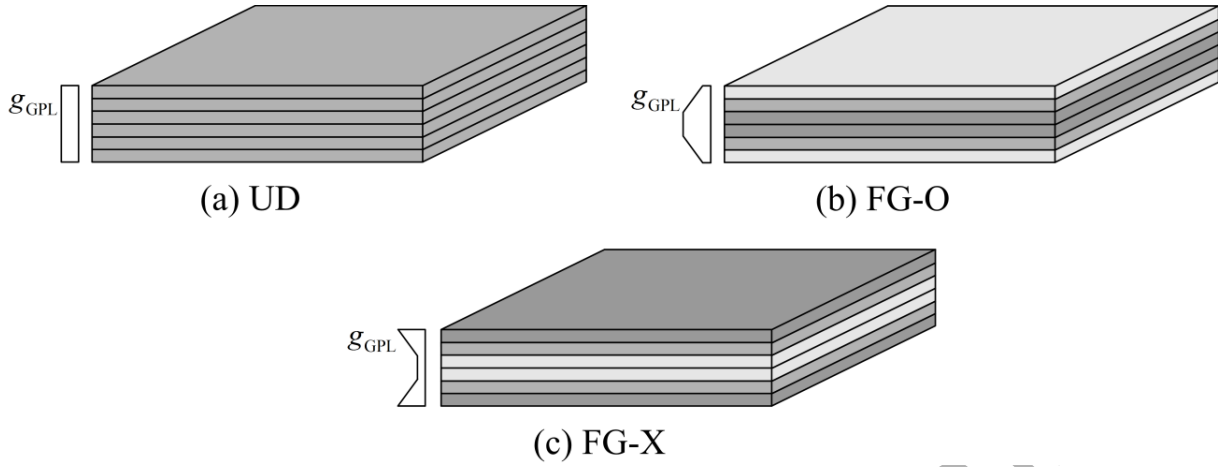
7

(a) UD

(b) FG-O

(c) FG-X

Fig. 2. Schematic diagrams of three GPL distribution patterns in the functionally graded multilayer GPLRC plates

2.1 Material Properties of GPLRCs

The effective Young's modulus and Poisson's ratio of the GPLRCs can be approximated by modified Halpin-Tsai model [27] and the rule of mixture, respectively, i.e.,

$$E_{\mathrm{C}} = \frac{3}{8} \frac{1 + \xi_{\mathrm{L}} \eta_{\mathrm{L}} V_{\mathrm{GPL}}}{1 - \eta_{\mathrm{L}} V_{\mathrm{GPL}}} \times E_{\mathrm{M}} + \frac{5}{8} \frac{1 + \xi_{\mathrm{W}} \eta_{\mathrm{W}} V_{\mathrm{GPL}}}{1 - \eta_{\mathrm{W}} V_{\mathrm{GPL}}} \times E_{\mathrm{M}} \tag{1}$$

$$\nu_{\mathrm{C}} = \nu_{\mathrm{GPL}} V_{\mathrm{GPL}} + \nu_{\mathrm{M}} \left(1 - V_{\mathrm{GPL}}\right) \tag{2}$$

where

$$\eta_{\mathrm{L}} = \frac{(E_{\mathrm{GPL}}/E_{\mathrm{M}}) - 1}{(E_{\mathrm{GPL}}/E_{\mathrm{M}}) + \xi_{\mathrm{L}}} \tag{3}$$

$$\eta_{\mathrm{W}} = \frac{(E_{\mathrm{GPL}}/E_{\mathrm{M}}) - 1}{(E_{\mathrm{GPL}}/E_{\mathrm{M}}) + \xi_{\mathrm{W}}} \tag{4}$$

Subscripts "GPL" and "M" stand for GPLs and polymer matrix, respectively, and ξ_{L} and ξ_{W} are the parameters characterizing both the geometry and size of GPL naofillers, defined as

8

$$\xi_L = 2\left(\frac{l_{\mathrm{GPL}}}{h_{\mathrm{GPL}}}\right), \quad \xi_{\mathrm{W}} = 2\left(\frac{w_{\mathrm{GPL}}}{h_{\mathrm{GPL}}}\right) \tag{5}$$

in which l_{GPL}, w_{GPL} and h_{GPL} are the average length, width, and thickness of the GPLs, respectively. The volume fraction of GPLs is given by

$$V_{\mathrm{GPL}} = \frac{g_{\mathrm{GPL}}}{g_{\mathrm{GPL}} + (\rho_{\mathrm{GPL}}/\rho_{\mathrm{M}})(1 - g_{\mathrm{GPL}})} \tag{6}$$

where g_{GPL} is GPL weight fraction, ρ_{M} and ρ_{GPL} are the mass densities of polymer matrix and GPLs, respectively.

Without the loss of generality, in this study *N* is assumed to be an even number and the GPL weight fraction of the *k*th layer for the three GPL distribution patterns are given as Ref. [27], i.e.,

$$\text{UD:} \quad g_{\mathrm{GPL}}^{(k)} = g_{\mathrm{GPL}}^{*} \tag{7}$$

$$\text{FG-O:} \quad g_{\mathrm{GPL}}^{(k)} = 4g_{\mathrm{GPL}}^{*}\left(\frac{N+1}{2} - \left|k - \frac{N+1}{2}\right|\right)/(2+N) \tag{8}$$

$$\text{FG-X:} \quad g_{\mathrm{GPL}}^{(k)} = 4g_{\mathrm{GPL}}^{*}\left(\frac{1}{2} + \left|k - \frac{N+1}{2}\right|\right)/(2+N) \tag{9}$$

in which g_{GPL}^{*} is the total GPL weight fraction.

2.2 Governing Equation

According to the FSDT [35], the displacements of an arbitrary point in the plate along the *X*-, *Y*- and *Z*- directions are written as

$$\begin{aligned}
u(X,Y,Z) &= \bar{U}(X,Y) + Z\bar{\phi}_x(X,Y) \\
v(X,Y,Z) &= \bar{V}(X,Y) + Z\bar{\phi}_y(X,Y) \\
w(X,Y,Z) &= \bar{W}(X,Y) + \bar{W}^{*}(X,Y)
\end{aligned} \tag{10}$$

9

where $\bar{U}(X,Y)$, $\bar{V}(X,Y)$ and $\bar{W}(X,Y)$ are displacement components of a point at the mid-plane of the plate, $\bar{\phi}_x$ and $\bar{\phi}_y$ are the rotations of a transverse normal about the *Y*- and *X*-axes, and $\bar{W}^*$ is a given small imperfection representing a small initial deviation of the plate plane from a flat shape.

In the absence of body forces, the equations of equilibrium of an imperfect laminated plate are

$$\frac{\partial N_x}{\partial X} + \frac{\partial N_{xy}}{\partial Y} = 0 \tag{11}$$

$$\frac{\partial N_{xy}}{\partial X} + \frac{\partial N_y}{\partial Y} = 0 \tag{12}$$

$$\frac{\partial Q_x}{\partial X} + \frac{\partial Q_y}{\partial Y} + \frac{\partial}{\partial X}\left[N_x \frac{\partial}{\partial X}(\bar{W}+\bar{W}^*) + N_{xy}\frac{\partial}{\partial Y}(\bar{W}+\bar{W}^*)\right] +$$
$$\frac{\partial}{\partial Y}\left[N_{xy}\frac{\partial}{\partial X}(\bar{W}+\bar{W}^*) + N_y\frac{\partial}{\partial Y}(\bar{W}+\bar{W}^*)\right] = 0 \tag{13}$$

$$\frac{\partial \bar{M}_x}{\partial X} + \frac{\partial \bar{M}_{xy}}{\partial Y} - Q_x = 0 \tag{14}$$

$$\frac{\partial \bar{M}_{xy}}{\partial X} + \frac{\partial \bar{M}_y}{\partial Y} - Q_y = 0 \tag{15}$$

where stress resultants $\mathbf{N} = \left[N_x, N_y, N_{xy}\right]^T$, shear forces $\mathbf{Q} = \left[Q_y, Q_x\right]^T$, and moment resultants $\bar{\mathbf{M}} = \left[\bar{M}_x, \bar{M}_y, \bar{M}_{xy}\right]^T$ are defined by

$$\left\{\begin{array}{c}\mathbf{N}\\ \bar{\mathbf{M}}\end{array}\right\} = \begin{bmatrix}\mathbf{A} & \mathbf{B}\\ \mathbf{B} & \mathbf{D}\end{bmatrix}\left\{\begin{array}{c}\boldsymbol{\varepsilon}^0\\ \boldsymbol{\varepsilon}^1\end{array}\right\} \tag{16}$$

$$\mathbf{Q} = k_S \mathbf{K}\boldsymbol{\gamma}^{(0)} \tag{17}$$

where $k_S = 5/6$ is the shear correction factor. The stiffness components A_{ij}, B_{ij}, D_{ij} and K_{ij} are calculated by

10

$$(A_{ij}, B_{ij}, D_{ij}) = \sum_{k=1}^{N} \int_{z_k}^{z_{k+1}} P_{ij}^{(k)}(1, z, z^2)\mathrm{d}z, \quad (i, j = 1, 2, 3) \tag{18}$$

$$K_{ij} = \sum_{k=1}^{N} \int_{z_k}^{z_{k+1}} Q_{ij}^{(k)}\mathrm{d}Z, \quad (i, j = 1, 2) \tag{19}$$

in which

$$P_{11}^{(k)} = P_{22}^{(k)} = \frac{E_C^{(k)}}{1-\nu^{(k)2}}, \quad P_{12}^{(k)} = P_{21}^{(k)} = \frac{\nu^{(k)}E_C^{(k)}}{1-\nu^{(k)2}}, \quad P_{33}^{(k)} = Q_{11}^{(k)} = Q_{22}^{(k)} = \frac{E_C^{(k)}}{2(1+\nu^{(k)})}, \tag{20}$$
$$P_{13}^{(k)} = P_{31}^{(k)} = P_{23}^{(k)} = P_{32}^{(k)} = Q_{12}^{(k)} = Q_{21}^{(k)} = 0$$

As the in-plane displacements *u* and *v* are small compared to the transverse displacement *w* and the higher-order terms are negligible, the von Kármán type nonlinear strains that are associated with the displacement field in Eq. (7) are given by

$$\boldsymbol{\varepsilon}^{(0)} = \left\{ \begin{array}{c} \varepsilon_{xx}^{(0)} \\ \varepsilon_{yy}^{(0)} \\ \gamma_{xy}^{(0)} \end{array} \right\} = \left\{ \begin{array}{c} \dfrac{\partial \bar{U}}{\partial X} + \dfrac{1}{2}\left(\dfrac{\partial \bar{W}}{\partial X}\right)^2 + \dfrac{\partial \bar{W}}{\partial X}\dfrac{\partial \bar{W}^*}{\partial X} \\ \dfrac{\partial \bar{V}}{\partial Y} + \dfrac{1}{2}\left(\dfrac{\partial \bar{W}}{\partial Y}\right)^2 + \dfrac{\partial \bar{W}}{\partial Y}\dfrac{\partial \bar{W}^*}{\partial Y} \\ \dfrac{\partial \bar{U}}{\partial Y} + \dfrac{\partial \bar{V}}{\partial X} + \dfrac{\partial \bar{W}}{\partial X}\dfrac{\partial \bar{W}}{\partial Y} + \dfrac{\partial \bar{W}}{\partial X}\dfrac{\partial \bar{W}^*}{\partial Y} + \dfrac{\partial \bar{W}}{\partial Y}\dfrac{\partial \bar{W}^*}{\partial X} \end{array} \right\},$$

$$\boldsymbol{\varepsilon}^{(1)} = \left\{ \begin{array}{c} \varepsilon_{xx}^{(1)} \\ \varepsilon_{yy}^{(1)} \\ \gamma_{xy}^{(1)} \end{array} \right\} = \left\{ \begin{array}{c} \dfrac{\partial \bar{\phi}_x}{\partial X} \\ \dfrac{\partial \bar{\phi}_y}{\partial Y} \\ \dfrac{\partial \bar{\phi}_x}{\partial Y} + \dfrac{\partial \bar{\phi}_y}{\partial X} \end{array} \right\}, \quad \boldsymbol{\gamma}^{(0)} = \left\{ \begin{array}{c} \gamma_{yz}^{(0)} \\ \gamma_{xz}^{(0)} \end{array} \right\} = \left\{ \begin{array}{c} \bar{\phi}_y + \dfrac{\partial \bar{W}}{\partial Y} + \dfrac{\partial \bar{W}^*}{\partial Y} \\ \bar{\phi}_x + \dfrac{\partial \bar{W}}{\partial X} + \dfrac{\partial \bar{W}^*}{\partial X} \end{array} \right\} \tag{21}$$

Let $\bar{F}$ be the stress resultants such that $N_x = \bar{F}_{,YY}$, $N_y = \bar{F}_{,XX}$, and $N_{xy} = -\bar{F}_{,XY}$, where a comma denotes partial differentiation with respect to the coordinates. Relationship (16) can be rewritten in partial reverse form as

$$\left\{ \begin{array}{c} \boldsymbol{\varepsilon}^{(0)} \\ \bar{\mathbf{M}} \end{array} \right\} = \left[\begin{array}{cc} \mathbf{A}^* & \mathbf{B}^* \\ -(\mathbf{B}^*)^T & \mathbf{D}^* \end{array} \right] \left\{ \begin{array}{c} \mathbf{N} \\ \boldsymbol{\varepsilon}^{(1)} \end{array} \right\} \tag{22}$$

11

where $(\ )^T$ represents the transpose of the matrix, and $\mathbf{A}^* = \mathbf{A}^{-1}$, $\mathbf{B}^* = -\mathbf{A}^{-1}\mathbf{B}$, $\mathbf{D}^* = \mathbf{D} - \mathbf{B}\mathbf{A}^{-1}\mathbf{B}$.

Introducing the following dimensionless quantities

$$x = \pi \frac{X}{a}, \quad y = \pi \frac{Y}{b}, \quad \beta = \frac{a}{b}, \quad \Delta = \left(D_{11}^* D_{22}^* A_{11}^* A_{22}^* \right)^{\frac{1}{4}},$$

$$\left(W, W^* \right) = \frac{\left(\bar{W}, \bar{W}^* \right)}{\Delta}, \quad F = \frac{\bar{F}}{\left(D_{11}^* D_{22}^* \right)^{\frac{1}{2}}}, \quad \left(\phi_x, \phi_y \right) = \frac{a}{\pi} \frac{\left(\bar{\phi}_x, \bar{\phi}_y \right)}{\Delta}, \tag{23}$$

$$\gamma_5 = -\frac{A_{12}^*}{A_{22}^*}, \quad \left(M_x, M_y \right) = \frac{a^2}{\pi^2} \frac{\left(\bar{M}_x, \bar{M}_y \right)}{\Delta D_{11}^*}, \quad \left(\lambda_x, \lambda_y \right) = \frac{\left(N_x b, N_y a \right)}{4\pi^2 \left(D_{11}^* D_{22}^* \right)^{\frac{1}{2}}},$$

substituting Eqs. (21) and (22) into equilibrium Eqs. (11)-(15), and considering the conditions of the deformation compatibility of the plate

$$\frac{\partial^2 \varepsilon_{xx}^{(0)}}{\partial Y^2} + \frac{\partial^2 \varepsilon_{yy}^{(0)}}{\partial X^2} - \frac{\partial^2 \gamma_{xy}^{(0)}}{\partial X \partial Y} = \left(\frac{\partial^2 \bar{W}}{\partial X \partial Y} \right)^2 - \frac{\partial^2 \bar{W}}{\partial X^2} \frac{\partial^2 \bar{W}}{\partial Y^2}$$

$$+ 2\frac{\partial^2 \bar{W}}{\partial X \partial Y} \frac{\partial^2 \bar{W}^*}{\partial X \partial Y} - \frac{\partial^2 \bar{W}}{\partial X^2} \frac{\partial^2 \bar{W}^*}{\partial Y^2} - \frac{\partial^2 \bar{W}}{\partial Y^2} \frac{\partial^2 \bar{W}^*}{\partial X^2} \tag{24}$$

leads to the nonlinear governing equations for an imperfect functionally graded multilayer GPLRC plate in terms of W, ϕ_x, ϕ_y and F as follows

$$L_{11}(W) + L_{12}(\phi_x) + L_{13}(\phi_y) + \beta^2 L(W + W^*, F) = 0 \tag{25}$$

$$L_{21}(F) = -\frac{1}{2}\beta^2 L(W + 2W^*, W) \tag{26}$$

$$L_{31}(W) + L_{32}(\phi_x) + L_{33}(\phi_y) = 0 \tag{27}$$

$$L_{41}(W) + L_{42}(\phi_x) + L_{43}(\phi_y) = 0 \tag{28}$$

12

where the nonlinear partial differential operator $L( ) = ( )_{,xx}( )_{,yy} - 2( )_{,xy}( )_{,xy} + ( )_{,yy}( )_{,xx}$, L_{ij} are

linear partial differential operators and are given in Appendix A.

For a plate simply supported on all edges, the boundary conditions are

$x = 0, \pi$:

$$W = \phi_y = 0 \tag{29}$$

$$\frac{\partial^2 F}{\partial x \partial y} = M_x = 0 \tag{30}$$

$$4\lambda_x + \frac{1}{\pi}\int_0^\pi \frac{\partial^2 F}{\partial y^2}\,\mathrm{d}y = 0 \tag{31}$$

$y = 0, \pi$:

$$W = \phi_x = 0 \tag{32}$$

$$\frac{\partial^2 F}{\partial x \partial y} = M_y = 0 \tag{33}$$

$$4\lambda_y + \frac{1}{\pi}\int_0^\pi \frac{\partial^2 F}{\partial x^2}\,\mathrm{d}x = 0 \tag{34}$$

3. Analytical Method and Asymptotic Solutions

A two step perturbation technique [47] is employed to solve Eqs. (25)-(28) to determine the

postbuckling equilibrium paths of functionally graded multilayer GPLRC plates. The solutions of Eqs. (25)

-(28) are assumed to take the form of

$$W(x, y, \varepsilon) = \sum_{j=1} \varepsilon^j w_j(x, y), \quad F(x, y, \varepsilon) = \sum_{j=0} \varepsilon^j f_j(x, y),$$

$$\phi_x(x, y, \varepsilon) = \sum_{j=1} \varepsilon^j \varphi_{xj}(x, y), \quad \phi_y(x, y, \varepsilon) = \sum_{j=1} \varepsilon^j \varphi_{yj}(x, y), \tag{35}$$

where ε is a small perturbation parameter and $w_1(x, y)$ is assumed to have the form

$$w_1(x, y) = A_{11}^{(1)} \sin mx \sin ny \qquad (36)$$

and the initial geometric imperfection is assumed to have a similar form to w_1 :

$$W^*(x, y, \varepsilon) = \varepsilon a_{11}^* \sin mx \sin ny = \varepsilon \mu A_{11}^{(1)} \sin mx \sin ny \qquad (37)$$

in which $\mu = \dfrac{a_{11}^*}{A_{11}^{(1)}}$ is the imperfection parameter.

By substituting Eq. (35) into Eqs. (25)-(28) and collecting terms of the same order of ε and because w_j , f_j , φ_{xj} and φ_{yj} are independent of ε , one can set the coefficient of each power of ε equal to zero. This leads to the following set of equations:

Order ε^0 :

$$L_{21}(f_0) = 0 \qquad (38)$$

Order ε^1 :

$$L_{11}(w_1) + L_{12}(\varphi_{x1}) + L_{13}(\varphi_{y1}) + \beta^2 L((1+\mu)w_1, f_0) = 0 \qquad (39)$$

$$L_{21}(f_1) = 0 \qquad (40)$$

$$L_{31}(w_1) + L_{32}(\varphi_{x1}) + L_{33}(\varphi_{y1}) = 0 \qquad (41)$$

$$L_{41}(w_1) + L_{42}(\varphi_{x1}) + L_{43}(\varphi_{y1}) = 0 \qquad (42)$$

Order ε^2 :

$$L_{11}(w_2) + L_{12}(\varphi_{x2}) + L_{13}(\varphi_{y2}) + \beta^2 L(w_2, f_0) + \beta^2 L((1+\mu)w_1, f_1) = 0 \qquad (43)$$

14

$$L_{21}(f_2) = -\frac{1}{2}\beta^2 L((1+2\mu)w_1, w_1) \tag{44}$$

$$L_{31}(w_2) + L_{32}(\varphi_{x2}) + L_{33}(\varphi_{y2}) = 0 \tag{45}$$

$$L_{41}(w_2) + L_{42}(\varphi_{x2}) + L_{43}(\varphi_{y2}) = 0 \tag{46}$$

Order ε^3:

$$
\begin{aligned}
&L_{11}(w_3) + L_{12}(\varphi_{x3}) + L_{13}(\varphi_{y3}) + \beta^2 L(w_3, f_0) \\
&+ \beta^2 L(w_2, f_1) + \beta^2 L((1+\mu)w_1, f_2) = 0
\end{aligned} \tag{47}
$$

$$L_{21}(f_3) = -\frac{1}{2}\beta^2 L((1+2\mu)w_1, w_2) - \frac{1}{2}\beta^2 L(w_2, w_1) \tag{48}$$

$$L_{31}(w_3) + L_{32}(\varphi_{x3}) + L_{33}(\varphi_{y3}) = 0 \tag{49}$$

$$L_{41}(w_3) + L_{42}(\varphi_{x3}) + L_{43}(\varphi_{y3}) = 0 \tag{50}$$

Order ε^4:

$$
\begin{aligned}
&L_{11}(w_4) + L_{12}(\varphi_{x4}) + L_{13}(\varphi_{y4}) + \beta^2 L(w_4, f_0) \\
&+ \beta^2 L(w_3, f_1) + \beta^2 L(w_2, f_2) + \beta^2 L((1+\mu)w_1, f_3) = 0
\end{aligned} \tag{51}
$$

$$L_{21}(f_4) = -\frac{1}{2}\beta^2 L((1+2\mu)w_1, w_3) - \frac{1}{2}\beta^2 L(w_2, w_2) - \frac{1}{2}\beta^2 L(w_3, w_1) \tag{52}$$

$$L_{31}(w_4) + L_{32}(\varphi_{x4}) + L_{33}(\varphi_{y4}) = 0 \tag{53}$$

$$L_{41}(w_4) + L_{42}(\varphi_{x4}) + L_{43}(\varphi_{y4}) = 0 \tag{54}$$

Considering the boundary conditions in Eqs. (29)-(34), the solutions of w_j, f_j, φ_{xj} and φ_{yj} can be

obtained by solving Eqs. (38)-(54) from order ε^0 to ε^4. Then, the asymptotic solutions of the

displacements and stress function of the plate are constructed as:

15

$$w = \varepsilon A_{11}^{(1)} \sin mx \sin ny + \varepsilon^3 \left(A_{13}^{(3)} \sin mx \sin 3ny + A_{31}^{(3)} \sin 3mx \sin ny \right) + O(\varepsilon^5) \quad (55)$$

$$F = -b_{00}^{(0)} \frac{x^2}{2} - B_{00}^{(0)} \frac{y^2}{2} + \varepsilon^2 \left(-b_{00}^{(2)} \frac{x^2}{2} - B_{00}^{(2)} \frac{y^2}{2} + B_{20}^{(2)} \cos 2mx + B_{02}^{(2)} \cos 2ny \right)$$

$$+ \varepsilon^4 \left(-b_{00}^{(4)} \frac{x^2}{2} - B_{00}^{(4)} \frac{y^2}{2} + B_{20}^{(4)} \cos 2mx + B_{02}^{(4)} \cos 2ny + B_{22}^{(4)} \cos 2mx \cos 2ny \right. \quad (56)$$

$$\left. + B_{40}^{(4)} \cos 4mx + B_{04}^{(4)} \cos 4ny + B_{24}^{(4)} \cos 2mx \cos 4ny + B_{42}^{(4)} \cos 4mx \cos 2ny \right) + O(\varepsilon^6)$$

$$\phi_x = \varepsilon C_{11}^{(1)} \cos mx \sin ny + \varepsilon^3 \left(C_{13}^{(3)} \cos mx \sin 3ny + C_{31}^{(3)} \cos 3mx \sin ny \right) + O(\varepsilon^5) \quad (57)$$

$$\phi_y = \varepsilon D_{11}^{(1)} \sin mx \cos ny + \varepsilon^3 \left(D_{13}^{(3)} \sin mx \cos 3ny + D_{31}^{(3)} \sin 3mx \cos ny \right) + O(\varepsilon^5) \quad (58)$$

Coefficients in Eqs. (55)-(58) are given in Appendix B, except $b_{00}^{(k)}$ and $B_{00}^{(k)}$ ($k = 0, 2, 4, \ldots$) which satisfy

$$\beta^2 (1 + \mu) A_{11}^{(1)} \left(b_{00}^{(0)} n^2 + B_{00}^{(0)} m^2 \right) = \left(\gamma_{110} m^2 + \gamma_{112} n^2 \right) A_{11}^{(1)} + m \gamma_{120} C_{11}^{(1)} + n \gamma_{131} D_{11}^{(1)} \quad (59)$$

$$m^2 B_{00}^{(2)} + n^2 b_{00}^{(2)} = 2 m^2 n^2 \left(B_{02}^{(2)} + B_{20}^{(2)} \right) \quad (60)$$

$$\left(m^2 B_{00}^{(4)} + n^2 b_{00}^{(4)} \right) \beta^2 (1 + \mu) A_{11}^{(1)} = 2 \left(B_{02}^{(4)} + B_{20}^{(4)} \right) m^2 n^2 \beta^2 (1 + \mu) A_{11}^{(1)}$$

$$- 2 \left(A_{13}^{(3)} B_{02}^{(2)} + A_{31}^{(3)} B_{20}^{(2)} \right) m^2 n^2 \beta^2 \quad (61)$$

The postbuckling equilibrium paths of the plate under biaxial compression can then be obtained by substituting Eq. (56) into Eqs. (31) and (34)

$$4 \lambda_x = B_{00}^{(0)} + \varepsilon^2 B_{00}^{(2)} + \varepsilon^4 B_{00}^{(4)} + \ldots \quad (62)$$

$$4 \lambda_y = b_{00}^{(0)} + \varepsilon^2 b_{00}^{(2)} + \varepsilon^4 b_{00}^{(4)} + \ldots \quad (63)$$

Taking $(x, y) = (\pi / 2m, \pi / 2n)$, the dimensionless maximum deflection w_m can be obtained from Eq. (55):

$$w_m = \varepsilon A_{11}^{(1)} - \varepsilon^3 \left(A_{13}^{(3)} + A_{31}^{(3)} \right) + O(\varepsilon^5) \tag{64}$$

The inverse form of Eq. (64) can be written as

$$\varepsilon A_{11}^{(1)} = w_m + \left(\frac{g_{13}^A}{g_{13}} + \frac{g_{31}^A}{g_{31}} \right) w_m^3 \tag{65}$$

in which g_{13}^A, g_{31}^A, g_{13} and g_{31} are given in Appendix B. g_{13} and g_{31} are related to the coefficients $b_{00}^{(0)}$ and $B_{00}^{(0)}$ that need to be determined. Multiplying Eqs. (62) by m^2 and and (63) by n^2, using the relations in Eqs. (59)-(61) then replacing the perturbation parameter $\epsilon A_{11}^{(1)}$ with w_m, one can obtain

$$4\lambda_x m^2 + 4\lambda_y n^2 = \frac{g_{11}\gamma_{110}m^2 + g_{11}\gamma_{112}n^2 + m\gamma_{120}g_{11}^C + n\gamma_{131}g_{11}^D}{g_{11}\beta^2(1+\mu)}$$

$$+ \beta^2(1+2\mu)\left(\frac{m^4}{16\gamma_{214}} + \frac{n^4}{16} \right)w_m^2 \tag{66}$$

$$- \left[\left(\frac{g_{31}^A}{g_{31}}\frac{n^4}{8} + \frac{g_{13}^A}{g_{13}}\frac{m^4}{8\gamma_{214}} \right)\beta^2(1+\mu) + \frac{1+2\mu}{1+\mu}\left(\frac{g_{13}^A}{g_{13}}\frac{m^2}{16n^2\gamma_{214}} + \frac{g_{31}^A}{g_{31}}\frac{n^2}{16m^2} \right) \right]w_m^4$$

Setting $w_m = 0$ in Eq. (66), Eq. (66) can be simplified to

$$4g_{11}\beta^2(1+\mu)\left(\lambda_x m^2 + \lambda_y n^2 \right) = g_{11}\gamma_{110}m^2 + g_{11}\gamma_{112}n^2 + m\gamma_{120}g_{11}^C + n\gamma_{131}g_{11}^D \tag{67}$$

This formula is well known in the analysis of linear buckling of plates under biaxial compression. Usually, the compressive loads P_x and P_y vary proportionally, so that $\sigma_y = \alpha\sigma_x$. Hence

$$\alpha = \frac{\lambda_y}{\beta^2 \lambda_x} \tag{68}$$

where α is a constant. Substituting Eq. (68) into Eq. (66) leads to the postbuckling equilibrium path of the plate in terms of the dimensionless maximum deflection

17

$$\lambda_x = \lambda_x^{(0)} + \frac{1}{2}\lambda_x^{(2)}w_m^2 + \frac{1}{24}\lambda_x^{(4)}w_m^4 + O(\epsilon^6) \tag{69}$$

in which the postbuckling coefficients are

$$\lambda_x^{(0)} = \frac{g_{11}\gamma_{110}m^2 + g_{11}\gamma_{112}n^2 + m\gamma_{120}g_{11}^C + n\gamma_{131}g_{11}^D}{4g_{11}\beta^2(1+\mu)(m^2 + \alpha\beta^2 n^2)} \tag{70}$$

$$\lambda_x^{(2)} = \frac{\beta^2(1+2\mu)}{m^2 + \alpha\beta^2 n^2}\left(\frac{m^4}{32\gamma_{214}} + \frac{n^4}{32}\right) \tag{71}$$

$$\lambda_x^{(4)} = -\frac{1}{m^2 + \alpha\beta^2 n^2}\left[\left(\frac{g_{31}^A}{g_{31}}\frac{3n^4}{4} + \frac{g_{13}^A}{g_{13}}\frac{3m^4}{4\gamma_{214}}\right)\beta^2(1+\mu) + \frac{1+2\mu}{1+\mu}\left(\frac{g_{13}^A}{g_{13}}\frac{3m^2}{8n^2\gamma_{214}} + \frac{g_{31}^A}{g_{31}}\frac{3n^2}{8m^2}\right)\right]$$

$$\tag{72}$$

According to Eq. (68), the coefficients $b_{00}^{(k)}$ and $B_{00}^{(k)}$ in Eqs. (62) and (63) have the relation

$$b_{00}^{(k)} = \alpha\beta^2 B_{00}^{(k)}, \quad k = 0, 2, 4, \dots \tag{73}$$

Then, using Eq. (59) and (73), $b_{00}^{(0)}$ and $B_{00}^{(0)}$ can be determined

$$b_{00}^{(0)} = \frac{\alpha\left(g_{11}\gamma_{110}m^2 + g_{11}\gamma_{112}n^2 + m\gamma_{120}g_{11}^C + n\gamma_{131}g_{11}^D\right)}{g_{11}(1+\mu)(m^2 + \alpha\beta^2 n^2)} \tag{74}$$

$$B_{00}^{(0)} = \frac{g_{11}\gamma_{110}m^2 + g_{11}\gamma_{112}n^2 + m\gamma_{120}g_{11}^C + n\gamma_{131}g_{11}^D}{g_{11}\beta^2(1+\mu)(m^2 + \alpha\beta^2 n^2)} \tag{75}$$

and then the coefficients g_{13} and g_{31} can be determined. Eqs. (69)-(75) can be employed to perform numerical calculations to trace postbuckling equilibrium paths of functionally graded multilayer GPLRC plates under biaxial compression. It should be noted that Eq. (69) is also valid for the postbuckling analysis of GPLRC plates under uniaxial compression by setting $\alpha = 0$.

4. Numerical Results and Discussion

In this section, the buckling and postbuckling behaviors of functionally graded multilayer GPLRC plates subjected to biaxial edge compression are investigated. To ensure the accuracy and effectiveness of the present formulation and solution procedure, some validation studies will be presented. Thereafter, several tabular and graphical data will be presented to investigate the effects of distribution patterns, weight fraction, length-to-thickness and length-to-width ratios of GPL nanofillers on the buckling and postbuckling behaviors of GPLRC plates through a comprehensive parametric study.

4.1 Comparison studies

As there are no results available in open literature for the buckling and postbuckling analyses of functionally graded multilayer GPLRC plates, simply supported isotropic square plates subjected to unixial or equal biaxial compression are taken as examples to validate the present study. The dimensionless critical buckling loads $\lambda_{\mathrm{cr}} = N_{\mathrm{cr}} b / [\pi^2 (D_{11}^* D_{22}^*)^{\frac{1}{2}}]$ of perfect plates with different length-to-thickness ratio a/h are compared in Table 1 and Table 2 with existing results given in Refs. [48-52]. Moreover, the postbuckling equilibrium paths of perfect and imperfect plates are compared with the analytical solutions [53] and the experimental results [54] in Fig. 3, and the HSDPT solution [51] in Fig. 4, where $\bar{W}_c^* / h$ and $\bar{W}_c / h$ represent the dimensionless initial imperfection and deflection at the center of the plate, respectively. As can be observed, good agreement is achieved.

Table 1. Comparison of dimensionless buckling load ($\lambda_{\mathrm{cr}} = N_{\mathrm{cr}} b / [\pi^2 (D_{11}^* D_{22}^*)^{\frac{1}{2}}]$) for square plates ($\nu = 0.3$) under uniaxial compression

	a/h		
	5	10	20
Present	3.2637	3.7865	3.9444
Srinivas [48]	3.150	3.741	3.924
Reddy [49]	3.2653	3.7865	3.9443

19

Rao [50]	3.2637	3.7865	3.9444

Table 2. Comparison of dimensionless buckling load ($\lambda_{cr} = N_{cr}b / [\pi^2 (D_{11}^* D_{22}^*)^{\frac{1}{2}}]$)for square plates ($\nu = 0.3$) under equal biaxial compression

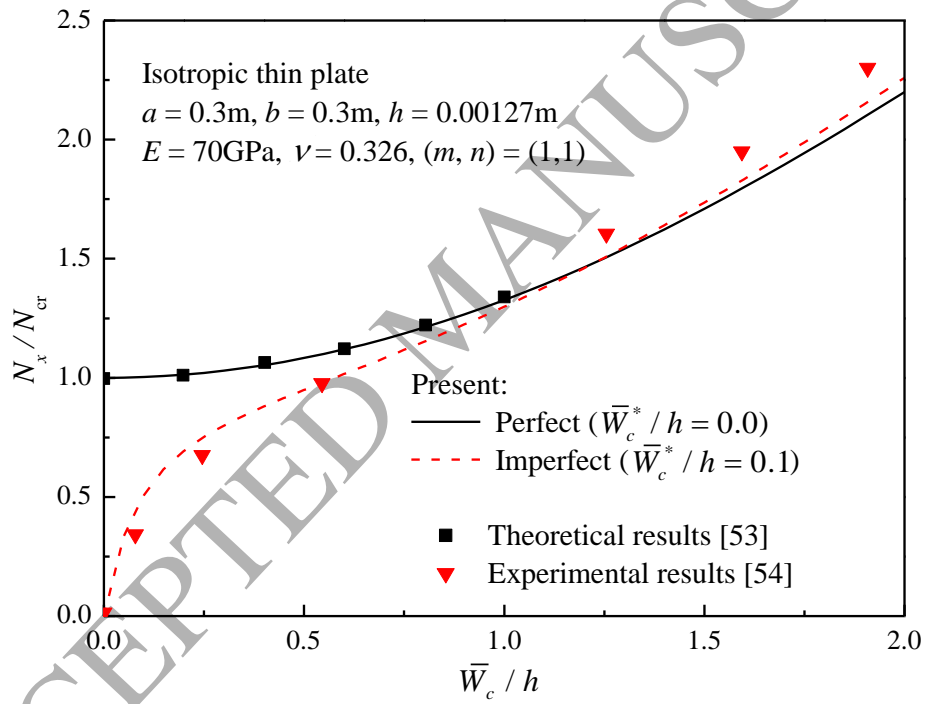|	a/h	
	10	20
Present	1.8932	1.9722
Bhimaraddi [51]	1.8936	1.9722
Xiang [52]	1.8920	1.9719

Fig. 3. Postbuckling equilibrium paths of simply supported perfect and imperfect isotropic plates under
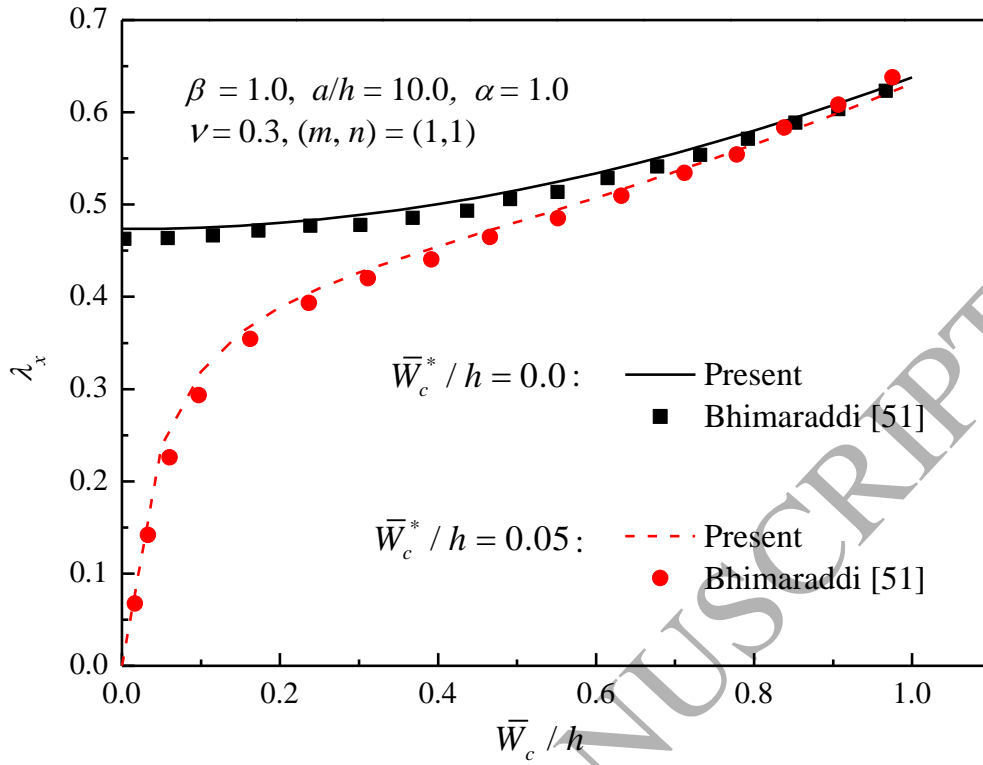
uniaxial compression

Fig. 4. Postbuckling equilibrium paths of simply supported perfect and imperfect isotropic square plates under equal biaxial compression

4.2 Parametric studies

In the following parametric studies, epoxy is chosen to be the matrix material. The geometric parameters of functionally graded GPLRC plates are $a = 0.45\text{m}$, $b = 0.45\text{m}$ and $h = 0.045\text{m}$, with the following material properties [17, 55, 56]:

$$\rho_{\text{M}} = 1.2\text{g/cm}^3, \qquad E_{\text{M}} = 3.0\text{GPa}, \qquad \nu_{\text{M}} = 0.34$$
$$\rho_{\text{GPL}} = 1.06\text{g/cm}^3, \quad E_{\text{GPL}} = 1.01\text{TPa}, \quad \nu_{\text{GPL}} = 0.186$$

Unless otherwise stated, the GPL weight fraction is 1.0% while its average length, width, and thickness are $l_{\text{GPL}} = 2.5\mu\text{m}$, $w_{\text{GPL}} = 1.5\mu\text{m}$, and $h_{\text{GPL}} = 1.5\text{nm}$ [17], respectively.

4.2.1 Buckling

21

Since bifurcation-type compressive buckling does not occur in an imperfect plate due to the bending-stretching coupling effect, in this section elastic buckling analysis will be conducted for perfect GPLRC plates only.

Table 3 investigates the effect of the total number of layers N on the critical buckling load ratio N_{cr}^{C} / N_{cr}^{M} for the GPLRC plates, in which N_{cr}^{C} and N_{cr}^{M} stand for critical buckling loads of the plates with and without GPLs, respectively. It should be noted that $\alpha < 0$, $\alpha = 0$ and $\alpha > 0$ correspond to the plate compressed in the *x*-coordinate but stretched in the *y*-coordinate, the plate uniaxially compressed in the *x*-coordinate, and the plate subjected to unequal biaxial compression, respectively. Due to the homogeneity, the critical buckling loads of UD plates are not affected by *N*, and their results are not listed in Table 3. As the total number of layers increases up to 10, for all values of α, the critical buckling loads increase for the FG-X plate but become lower for the FG-O plate then tend to be constants when $N \geq 10$. Hence, $N = 10$ is used in all the following numerical calculations.

Table 3. Effect of total number of layers on critical buckling load ratio (N_{cr}^{C} / N_{cr}^{M}) of functionally graded multilayer GPLRC plates under biaxial compression

	α	N								
		2	4	6	8	10	12	14	16	18
FG-O	1.0	4.3238	3.5317	3.2636	3.1288	3.0477	2.9935	2.9548	2.9257	2.9030
	0.5	4.3237	3.5316	3.2635	3.1288	3.0476	2.9934	2.9547	2.9256	2.9029
	0.0	4.3236	3.5315	3.2635	3.1287	3.0476	2.9934	2.9546	2.9255	2.9029
	-0.5	4.3236	3.5315	3.2635	3.1287	3.0476	2.9934	2.9546	2.9255	2.9029
FG-X	1.0	4.3238	5.0982	5.3525	5.4790	5.5546	5.6050	5.6409	5.6678	5.6887
	0.5	4.3237	5.0981	5.3524	5.4789	5.5545	5.6049	5.6408	5.6677	5.6886
	0.0	4.3236	5.0979	5.3523	5.4787	5.5544	5.6047	5.6406	5.6675	5.6885
	-0.5	4.3236	5.0979	5.3523	5.4787	5.5544	5.6047	5.6406	5.6675	5.6885

The effect of GPL weight fraction g_{GPL} on the critical buckling loads for GPLRC plates is presented in Table 4 where the value in parentheses denote the critical buckling load ratio. The results of the pure epoxy plate are also listed for comparison. As can be observed, GPL nanofillers even at a very low content can significantly improve the critical buckling loads of the plates. For example, by dispersing only 1.0 wt.% GPLs, the FG-X plate has much bigger critical buckling loads that are 555% of those of the pristine epoxy plate. It can also be observed that the critical buckling loads, which are remarkably improved as GPL weight fraction increases. Among the three GPL distribution patterns, for each value of α, FG-X offers the biggest critical buckling load while FG-O brings the lowest critical buckling load. This is due to the fact that a plate with more GPLs distributed close to the plate surfaces has a higher bending stiffness. Moreover, it can be observed that the critical buckling loads of the plates can significantly increase as the tensile force in the *y*-coordinate increases.

Table 4. Effect of GPL weight fraction on critical buckling load of functionally graded multilayer GPLRC plates under biaxial compression (kN)

	α	g_{GPL}					
		Pure Epoxy	0.2%	0.4%	0.6%	0.8%	1.0%
UD	1.0	1066.1	1775.5	2484.5	3193.2	3901.5	4609.6
			(1.6654)	(2.3305)	(2.9952)	(3.6596)	(4.3238)
	0.5	1421.5	2367.3	3312.6	4257.5	5202.0	6146.1
			(1.6654)	(2.3304)	(2.9951)	(3.6595)	(4.3237)
	0.0	2132.3	3550.9	4968.9	6386.3	7803.1	9219.2
			(1.6653)	(2.3303)	(2.9950)	(3.6595)	(4.3236)
	-0.5	4264.6	7101.8	9937.9	12772.6	15606.1	18438.4
			(1.6653)	(2.3303)	(2.9950)	(3.6595)	(4.3236)
FG-O	1.0	1066.1	1505.3	1942.3	2378.3	2813.9	3249.2
			(1.4120)	(1.8218)	(2.2309)	(2.6394)	(3.0477)

	0.5	1421.5	2007.1	2589.7	3171.1	3751.9	4332.2
			(1.4120)	(1.8218)	(2.2308)	(2.6394)	(3.0476)
	0.0	2132.3	3010.7	3884.5	4756.7	5627.8	6498.3
			(1.4119)	(1.8218)	(2.2308)	(2.6393)	(3.0476)
	-0.5	4264.6	6021.4	7769.1	9513.3	11255.6	12996.6
			(1.4119)	(1.8218)	(2.2308)	(2.6393)	(3.0476)
FG-X	1.0	1066.1	2040.7	3012.6	3983.2	4952.9	5921.8
			(1.9141)	(2.8258)	(3.7362)	(4.6458)	(5.5546)
	0.5	1421.5	2720.9	4016.7	5310.9	6603.8	7895.7
			(1.9141)	(2.8257)	(3.7361)	(4.6457)	(5.5545)
	0.0	2132.3	4081.3	6025.1	7966.3	9905.7	11843.6
			(1.9141)	(2.8256)	(3.7360)	(4.6456)	(5.5544)
	-0.5	4264.6	8162.7	12050.2	15932.6	19811.5	23687.2
			(1.9141)	(2.8256)	(3.7360)	(4.6456)	(5.5544)

Note: The value in parantheses denotes the critical buckling load ratio $N_{\mathrm{cr}}^{\mathrm{C}} / N_{\mathrm{cr}}^{\mathrm{M}}$

The important effects of GPL geometry and size on the buckling behavior of functionally graded multilayer GPLRC plates are investigated in Table 5. It can be seen that the critical buckling loads increase as the $l_{\mathrm{GPL}} / h_{\mathrm{GPL}}$ ratio increases. However, a further increase in $l_{\mathrm{GPL}} / h_{\mathrm{GPL}}$ when it goes beyond 2000 can slightly improve the buckling resistance of the plates. In addition, square shaped GPLs ($l_{\mathrm{GPL}} / w_{\mathrm{GPL}} = 1.0$) outperform the rectangular ones ($l_{\mathrm{GPL}} / w_{\mathrm{GPL}} = 3.0$) in improving the critical buckling loads of the plates. Since l_{GPL} is kept constant here, this observation indicates that GPLs with a larger surface area are better reinforcing nanofillers than those with a smaller surface area. This is due to the fact that at the same GPL content, a larger contact area between the polymer matrix and the nanofillers provides better load transfer capacity.

Table 5. Effects of GPL length-to-thickness and length-to-width ratios on critical buckling load ratio

($N_{\mathrm{cr}}^{\mathrm{C}} / N_{\mathrm{cr}}^{\mathrm{M}}$) of functionally graded multilayer GPLRC plates under biaxial compression

	$l_{\mathrm{GPL}} / w_{\mathrm{GPL}}$	$l_{\mathrm{GPL}} / h_{\mathrm{GPL}} (\times 10^{-3})$	α			
			1.0	0.5	0.0	-0.5
UD	1.0	0.1	2.4287	2.4286	2.4286	2.4286
		0.5	3.8457	3.8456	3.8455	3.8455
		1.0	4.2502	4.2501	4.2500	4.2500
		1.5	4.4120	4.4119	4.4118	4.4118
		2.0	4.4992	4.4991	4.4989	4.4989
		2.5	4.5536	4.5535	4.5534	4.5534
		3.0	4.5909	4.5907	4.5906	4.5906
	3.0	0.1	1.9363	1.9362	1.9362	1.9362
		0.5	3.2554	3.2553	3.2552	3.2552
		1.0	3.8007	3.8006	3.8005	3.8005
		1.5	4.0581	4.0580	4.0579	4.0579
		2.0	4.2087	4.2086	4.2085	4.2085
		2.5	4.3078	4.3077	4.3076	4.3076
		3.0	4.3780	4.3779	4.3778	4.3778
FG-O	1.0	0.1	1.8814	1.8814	1.8813	1.8813
		0.5	2.7533	2.7533	2.7532	2.7532
		1.0	3.0024	3.0023	3.0023	3.0023
		1.5	3.1020	3.1020	3.1019	3.1019
		2.0	3.1557	3.1556	3.1555	3.1555
		2.5	3.1892	3.1892	3.1891	3.1891
		3.0	3.2122	3.2121	3.2120	3.2120
	3.0	0.1	1.5784	1.5784	1.5783	1.5783
		0.5	2.3901	2.3901	2.3900	2.3900
		1.0	2.7257	2.7256	2.7255	2.7255

		1.5	2.8841	2.8840	2.8840	2.8840
		2.0	2.9769	2.9768	2.9767	2.9767
		2.5	3.0379	3.0378	3.0377	3.0377
		3.0	3.0811	3.0810	3.0809	3.0809
FG-X	1.0	0.1	2.9650	2.9649	2.9648	2.9648
		0.5	4.9027	4.9026	4.9025	4.9025
		1.0	5.4544	5.4543	5.4542	5.4542
		1.5	5.6749	5.6748	5.6746	5.6746
		2.0	5.7936	5.7934	5.7933	5.7933
		2.5	5.8677	5.8676	5.8674	5.8674
		3.0	5.9184	5.9183	5.9182	5.9182
	3.0	0.1	2.2891	2.2891	2.2890	2.2890
		0.5	4.0961	4.0960	4.0959	4.0959
		1.0	4.8410	4.8409	4.8408	4.8408
		1.5	5.1923	5.1922	5.1920	5.1920
		2.0	5.3978	5.3976	5.3975	5.3975
		2.5	5.5328	5.5327	5.5326	5.5326
		3.0	5.6284	5.6283	5.6282	5.6282

4.2.2 Postbuckling

In this section, postbuckling analysis will be conducted for both perfect and imperfect functionally graded multilayer GPLRC plates.

Fig. 5 investigates the effect of the total number of layers *N* on the equal biaxial compressive postbuckling load ratio $N_x^{\mathrm{C}} / N_x^{\mathrm{M}}$ of perfect GPLRC plates, in which N_x^{C} and N_x^{M} stand for the postbuckling loads of the plates with and without GPLs, respectively. The dimensionless central deflection is taken as $\bar{W}_c / h = 1$. As the total number of layers increases up to 10, the postbuckling load

increases for the FG-X plate but becomes lower for the FG-O plate then tends to be constant when $N \geq 10$. The effect of the total number of layers *N* on the postbuckling load-deflection curves for the GPLRC plates with and without an initial imperfection are also investigated. The dimensionless load parameter $\lambda_0 = N_x b / (E_M h^3)$ against the dimensionless central deflection $\bar{W}_c / h$ results are presented in Fig. 6 for FG-X plates only for brevity since those for UD and FG-O plates are quite similar, all showing that 10 layers can achieve convergent results for the postbuckling response of the GPLRC plates. This is consistent with the results in buckling analysis and the observations in Ref. [27], indicating that a multilayer structure with a total of 10 layers stacked up together can well approximate the ideal functionally graded plate with a continuous and smooth through-thickness gradient in GPL distribution which is extremely difficult and expensive to be fabricated due to the limitation of current manufacturing technology. It can also been seen that the postbuckling load-deflection curves of the imperfect plates originate from the origin, which means that the imperfect plate starts to deflect even under a very small compressive force hence no bifurcation buckling exists even though the through-thickness material composition of the imperfect plate is symmetric about the mid-plane. The postbuckling load-deflection curves of the perfect and imperfect plates with the same value of *N* approach to each other as the deflection increases. The two load-deflection curves for the perfect and imperfect plates correspond to a smaller *N* approach each other much faster than those of the plates correspond to a larger *N*.
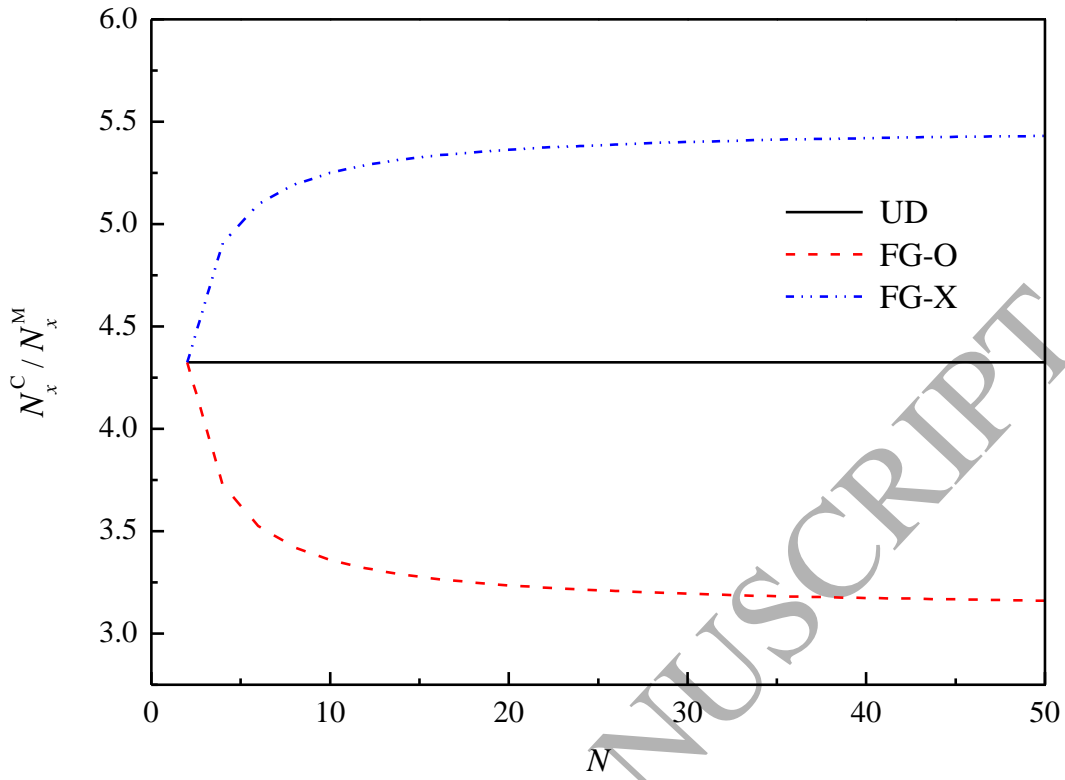
Fig. 5 Postbuckling load ratio $N_x^{\mathrm{C}}/N_x^{\mathrm{M}}$ at $\bar{W}_c/h=1$ for functionally graded multilayer GPLRC plates

under equal biaxial compression: Effect of total number of layers.
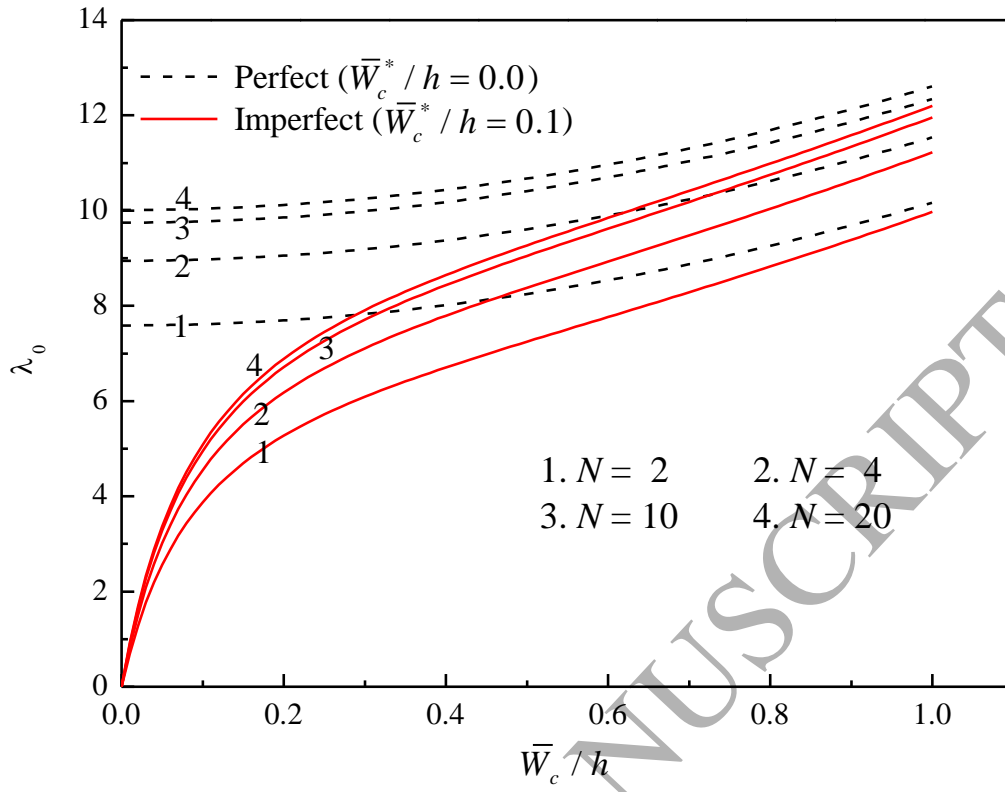
Fig. 6 Postbuckling equilibrium paths of functionally graded multilayer GPLRC plates under equal biaxial

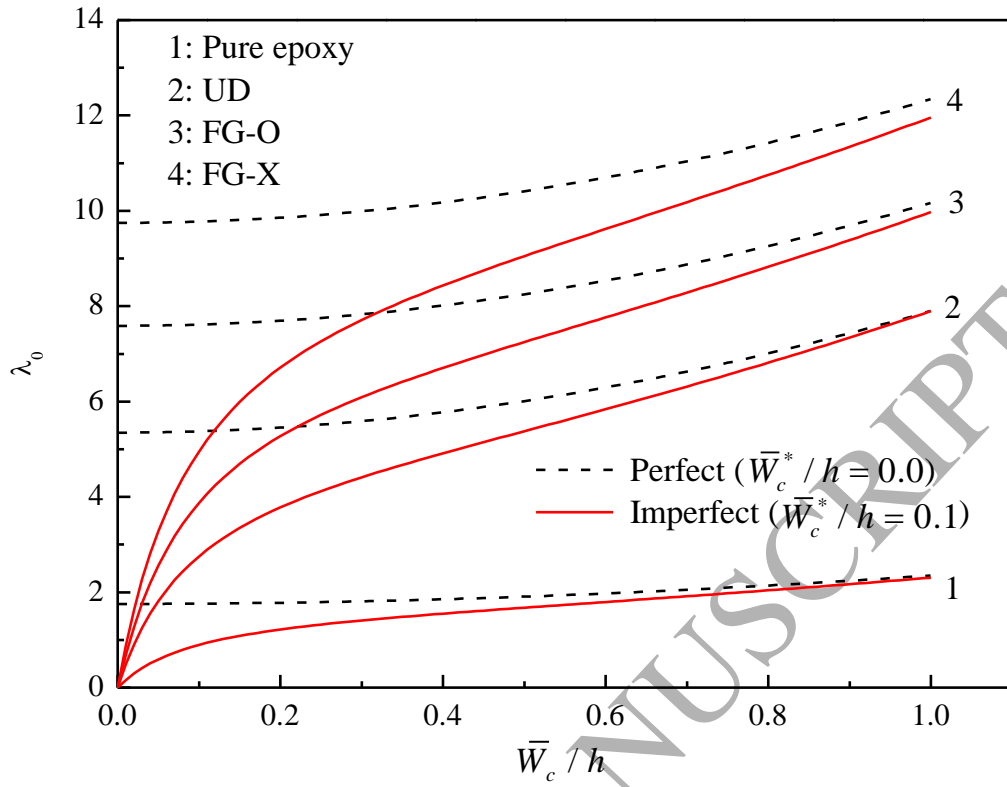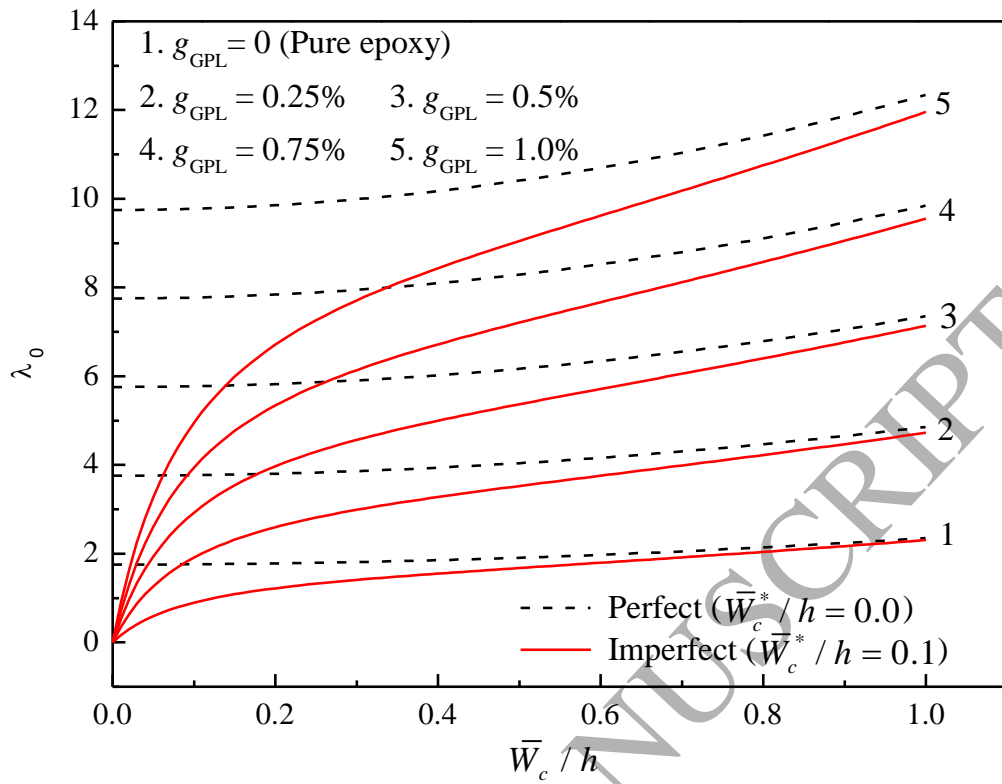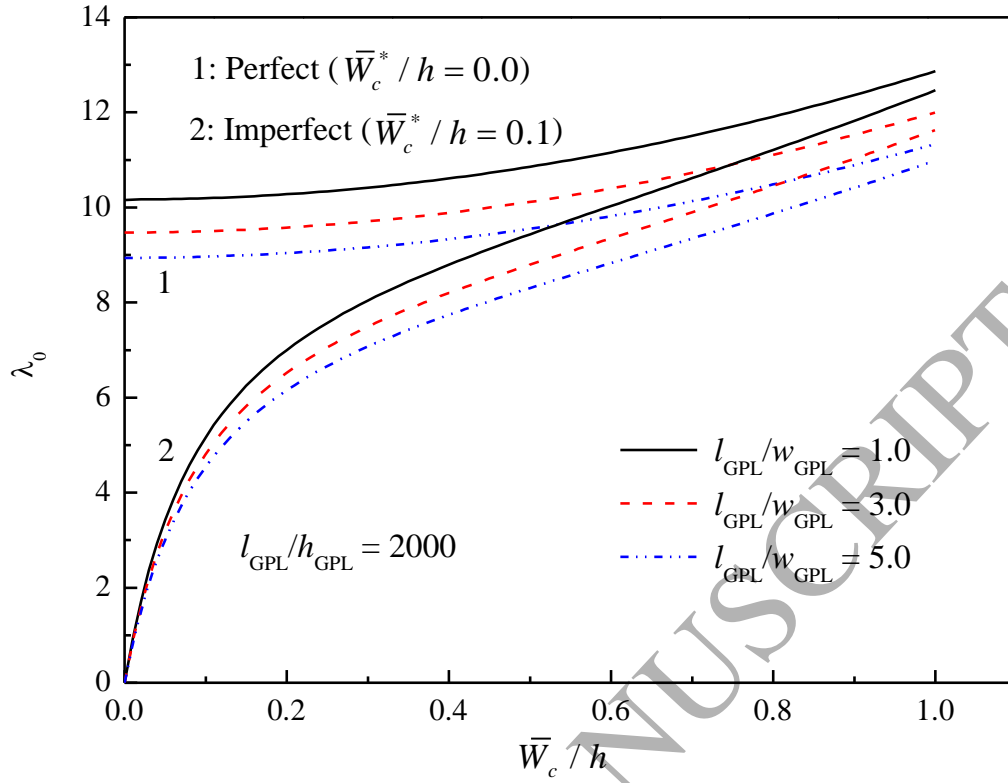compression: Effect of different total number of layers.

Fig. 7. Postbuckling equilibrium paths of functionally graded multilayer GPLRC plates under equal biaxial compression: Effect of GPL distribution pattern.

Fig. 7 displays the effect of GPL distribution pattern on the postbuckling response of functionally graded multilayer GPLRC plates under equal biaxial compression. Compared with the pure epoxy plate, all GPL-reinforced composite plates exhibit considerably higher postbuckling load-carrying capacity. It is apparent that, among the three GPL distributions considered, the postbuckling load-carrying capacity is the maximum for the FG-X plate and the minimum for the FG-O plate while the postbuckling load-deflection curve for the UD plate lies in between those for the FG-X and FG-O plates.

Fig. 8. Postbuckling equilibrium paths of functionally graded multilayer GPLRC plates under equal biaxial compression: Effect of GPL weight fractions

Fig. 8 depicts the effect of GPL weight fraction on the postbuckling load-deflection curves for FG-X plates under equal biaxial compression, showing that a remarkably improved postbuckling resistance can be achieved as the weight fraction g_{GPL} increases. For example, the addition of only 0.25% weight fraction GPLs can yield a significantly higher postbuckling resistance that is almost twice of that of the pure epoxy plate.

31
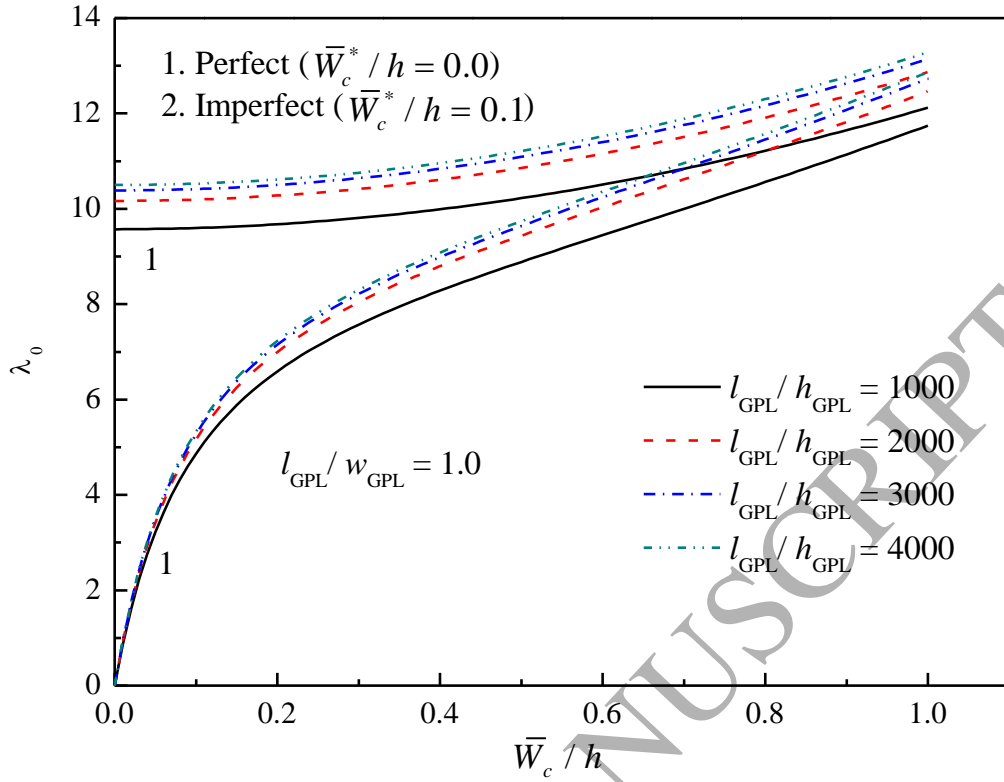
Fig. 9. Postbuckling equilibrium paths of functionally graded multilayer GPLRC plates under equal biaxial

compression: Effect of GPL length-to-width ratio

The effects of GPL length-to-thickness and length-to-width ratios on the postbuckling behavior of

functionally graded multilayer GPLRC plates are investigated in Fig. 9 which compares the postbuckling

load-deflection curves of FG-X plates with $l_{\mathrm{GPL}} / w_{\mathrm{GPL}}$ = 1.0, 3.0, 5.0 and $l_{\mathrm{GPL}} / h_{\mathrm{GPL}} = 2000$. Results

show that the postbuckling load-carrying capacity of the functionally graded GPLRC plate is the highest

when square shaped GPLs ($l_{\mathrm{GPL}} / w_{\mathrm{GPL}} = 1.0$) are used but becomes lower as $l_{\mathrm{GPL}} / w_{\mathrm{GPL}}$ increases.

Fig. 10. Postbuckling equilibrium paths of functionally graded multilayer GPLRC plates under equal biaxial compression: Effect of GPL length-to-thickness ratio.

Fig. 10 shows the postbuckling equilibrium paths of a FG-X plate reinforced with square GPLs having different length-to-thickness ratio $l_{\mathrm{GPL}}/h_{\mathrm{GPL}}$. Fig. 11 gives the postbuckling load ratio $N_x^{\mathrm{C}}/N_x^{\mathrm{M}}$ for perfect GPLRC plates when the dimensionless central deflection $\bar{W}_c/h = 1$. As can be observed, postbuckling load-deflection curve tends to be higher with an increasing $l_{\mathrm{GPL}}/h_{\mathrm{GPL}}$. This clearly indicates that GPLs with fewer layers are more effective in improving plate stiffness and its postbuckling resistance. However, when $l_{\mathrm{GPL}}/h_{\mathrm{GPL}}$ goes beyond 2000, the postbuckling resistance tends to be unchanged and the effects of $l_{\mathrm{GPL}}/w_{\mathrm{GPL}}$ and $l_{\mathrm{GPL}}/h_{\mathrm{GPL}}$ become much less significant.
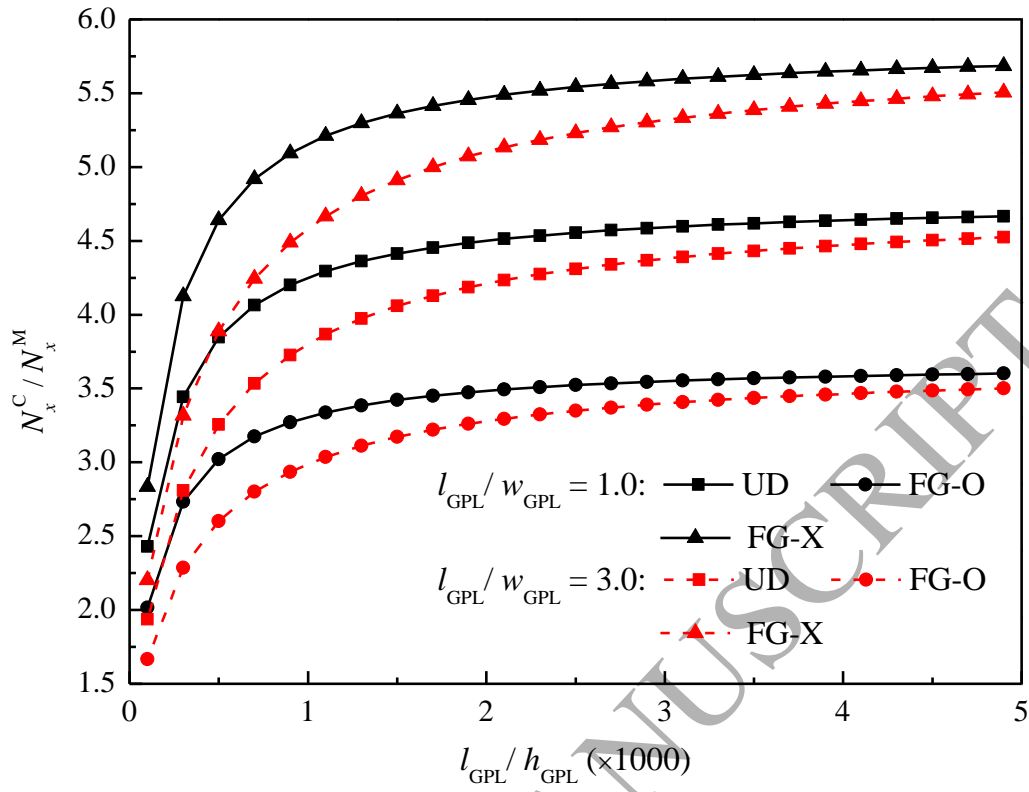
Fig. 11. Postbuckling load ratio $N_x^{\mathrm{C}} / N_x^{\mathrm{M}}$ for functionally graded multilayer GPLRC plates under equal

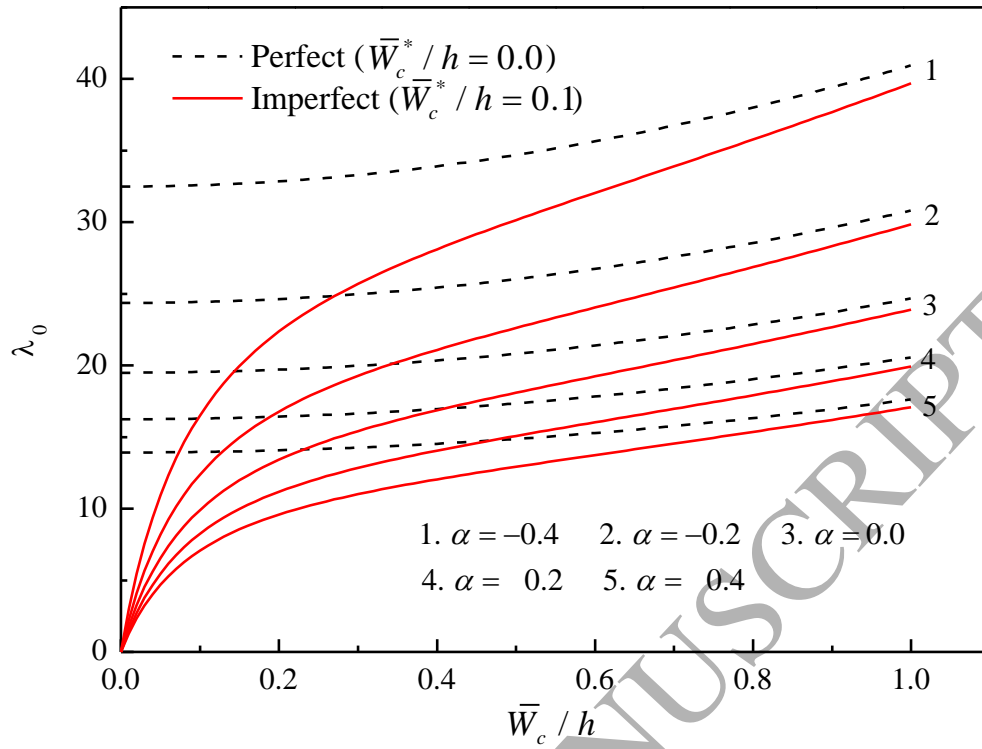biaxial compression when $\overline{W}_c / h = 1$: Effects of GPL length-to-thickness and length-to-width ratios.

Fig. 12 Postbuckling equilibrium paths of functionally graded multilayer GPLRC plates under biaxial

compression loads with different α

Fig. 12 investigates the postbuckling behavior of functionally graded GPLRC plates under different

loadings. Compared with the uniaxially compressed plate, the application of a bigger tensile force in the

y-coordinate can significantly increase the postbuckling resistance of the plate while the presence of a

larger compressive force in the *y*-coordinate leads to considerably reduced postbuckling resistance.

5. **Conclusions**

The buckling and postbuckling analysis of functionally graded multilayer GPLRC plates under biaxial

compression have been investigated using a two step perturbation technique. GPLs are uniformly

dispersed in the polymer matrix in each individual layer. The material properties of the plates are

assumed to be graded along the thickness direction since the GPL weight fraction shows a layer-wise

change, and are evaluated through micromechanics models. Based on the assumption that the

laminated plate is composed perfectly bonded GPLRC layers, equilibrium and compatibility equations for the composite plates are derived by using the first-order shear deformation plate theory taking into account both geometrical nonlinearity in von Kármán sense and initial geometrical imperfection. Numerical results have revealed that by dispersing a very small amount of GPLs into the polymer matrix can significantly improve the critical buckling load and postbuckling load-carrying capacity of the plates. Among the three GPL distribution patterns presented in this study, FG-X is the best way of dispersing GPLs that results in the highest critical buckling load and postbuckling load-carrying capacity. Furthermore, square GPLs with fewer monolayer graphene sheets are the most favorable reinforcing nanofillers.

Acknowledgements

References

[1] Suresh S, Mortensen A. Fundamentals of Functionally Graded Materials: Processing and thermomechanical behavior of graded metals and metal-ceramic composites. London: IOM Communications Ltd; 1998.

[2] Lee Y-D, Erdogan F. Residual/thermal stresses in FGM and laminated thermal barrier coatings. International Journal of Fracture 1994; 69 (2): 145-165.

[3] Pompe W, Worch H, Epple M, Friess W, Gelinsky M, Greil P, Hempel U, Scharnweber D, Schulte K. Functionally graded materials for biomedical applications. Materials Science and Engineering A 2003; 362: 40-60.

[4] Ichikawa K. (ed.). Functionally graded materials in the 21st Century: A workshop on trends and forecasts. Kluwer Academic Publishers; 2000.

[5] Lau KT, Hui D. The revolutionary creation of new advanced materials-Carbon nanotube composites. Composites Part B 2002;33: 263-277.

[6] Shen H-S. Nonlinear bending of functionally graded carbon nanotube-reinforced composite plates in thermal environments. Composite Structures 2009, 91: 9-19.

[7] Ke LL, Yang J, Kitipornchai S. Nonlinear free vibration of functionally graded carbon nanotube-reinforced composite beams. Composite Structures 2010; 92 (3): 676-683

[8] Shen H-S. Thermal buckling and postbuckling behavior of functionally graded carbon nanotube-reinforced composite cylindrical shells. Composites: Part B 2012; 43(3): 1030-1038.

[9] Ke LL, Yang J, Kitipornchai S. Dynamic stability of functionally graded carbon nanotube-reinforced composite beams. Mechanics of Advanced Materials and Structures. 2013; 20 (1): 28-37.

[10] Zhang LW, Lei ZX, Liew KM. Free vibration analysis of functionally graded carbon nanotube-reinforced composite triangular plates using the FSDT and element-free IMLS-Ritz method. Composite Structures 2015; 120: 189-199.

[11] Zhang LW, Zhang Y, Zou GL, Liew KM. Free vibration analysis of triangular CNT-reinforced composite plates subjected to in-plane stresses using FSDT element-free method. Composite Structures 2016; 149: 247-260.

[12] Zhang LW. On the study of the effect of in-plane forces on the frequency parameters of CNT-reinforced composite skew plates. Composite Structures 2017; 160: 824-837.

[13] Wu HL, Kitipornchai S, Yang J. Thermo-electro-mechanical postbuckling of piezoelectric FG-CNTRC beams with geometric imperfections. Smart Materials and Structures. 2016; 25(9): Art. No. 095022.

[14] Rafiee M, Yang J, Kitipornchai S. Thermal bifurcation buckling of piezoelectric carbon nanotube reinforced composite beams. Computers and Mathematics with Applications. 2013; 66 (7): 1147-1160.

[15] Ansari R, Shojaei MF, Mohammadi V, Gholami R, Sadeghi F. Nonlinear forced vibration analysis of functionally graded carbon nanotube-reinforced composite Timoshenko beams. Composite Structures 2014; 113: 316-327.

[16] Novoselov KS, Geim AK, Morozov SV, Jiang D, Zhang Y, Dubonos SV, et al. Electric field effect in atomically thin carbon films. Science 2004; 306:666-669.

[17] Rafiee MA, Rafiee J, Wang Z, Song H, Yu Z-Z, Koratkar N. Enhanced mechanical properties of nanocomposites at low graphene content. ACS Nano 2009; 3(12): 3884-3890.

[18] Fang M, Wang K, Lu H, Yang Y, Nutt S. Covalent polymer functionalization of graphene nanosheets and mechanical properties of composites. Journal of Materials Chemistry 2009; 19(38): 7098-7105.

[19] Zhao X, Zhang Q, Chen D, Lu P. Enhanced mechanical properties of graphene-based poly(vinyl alcohol) composites. Macromolecules 2010; 43(5): 2357-2363.

[20] Wang F, Drzal LT, Qin Y, Huang Z. Mechanical properties and thermal conductivity of graphene nanoplatelet/epoxy composites. Journal of Materials Science 2015; 50(3): 1082-1093.

[21] Ji X-Y, Cao Y-P, Feng X-Q. Micromechanics prediction of the effective elastic moduli of graphene sheet-reinforced polymer nanocomposites. Modelling and Simulation in Materials Science and Engineering 2010; 18(4): 045005.

[22] Rahman R, Haque A. Molecular modeling of crosslinked graphene-epoxy nanocomposites for characterization of elastic constants and interfacial properties. Composites: Part B 2013; 54: 353-364.

[23] Montazeri A, Rafii-Tabar H. Multiscale modeling of graphene- and nanotube-based reinforced polymer nanocomposites. Physics Letters A 2011; 375(45): 4034-4040.

[24] Chandra Y, Chowdhury R, Scarpa F, Adhikari S, Sienz J, Arnold C, Murmu T, Bould D. Vibration frequency of graphene based composites: A multiscale approach. Materials Science and Engineering B 2012; 177(3): 303-310.

[25] Cranford SW. Buckling induced delamination of graphene composites through hybrid molecular modeling. Applied Physics Letters 2013; 102: 031902.

[26] Rissanou AN, Power AJ, Harmandaris V. Structural and dynamical properties of polyethylene/graphene nanocomposites through molecular dynamics simulations. Polymers 2015; 7(3): 390-417.

[27] Song MT, Kitipornchai S, Yang J. Free and forced vibrations of functionally graded polymer composite plates reinforced with graphene nanoplatelets. Composite Structures 2017; 159: 579-588.

[28] Feng C, Kitipornchai S, Yang J. Nonlinear bending of polymer nanocomposite beams reinforced with non-uniformly distributed graphene platelets (GPLs). Composites Part B 2017; 110: 132-140.

[29] Yang J, Wu HL, Kitipornchai S. Buckling and postbuckling of functionally graded multilayer graphene platelet-reinforced composite beams. Composite Structures 2017; 161: 111-118.

[30] Wu HL, Yang J, Kitipornchai S. Dynamic stability of functionally graded multilayer graphene nanocomposite beams in thermal environment. Composite Structures 2017; 162: 244-254.

[31] Feng C, Kitipornchai S, Yang J. Nonlinear free vibration of functionally graded polymer composite beams reinforced with graphene nanoplatelets (GPLs). Engineering Structures. 2017; 140: 110-119.

[32] Chen D, Yang J, Kitipornchai S. Nonlinear vibration and postbuckling of functionally graded graphene reinforced porous nanocomposite beams. Composites Science and Technology. 2017; 142: 235-245.

[33] Shen HS, Xiang Y, Lin F. Nonlinear vibration of functionally graded graphene-reinforced composite laminated plates in thermal environments. Computer Methods in Applied Mechanics and Engineering 2017; 319 (1): 175–193.

[34] Shen HS, Xiang Y, Lin F. Nonlinear bending of functionally graded graphene-reinforced composite laminated plates resting on elastic foundations in thermal environments. Composite Structures 2017; 170: 80–90.

[35] Reddy JN. Mechanics of laminated composite plates and shells: theory and analysis. CRC Press; 2004.

[36] Shi GY. A new simple third-order shear deformation theory of plates. International Journal of Solids and Structures 2007; 44: 4399-4417.

[37] Bui TQ, Do TV, Ton LHT, Doan DH, Tanaka S, Pham DT, Nguyen-Van T-A, Yu TT, Hirose S. On the high temperature mechanical behaviors analysis of heated functionally graded plates using FEM and a new third-order shear deformation plate theory. Composites Part B 2016; 92: 218-241.

[38] Yu TT, Yin SH, Bui TQ, Xia SF, Tanaka S, Hirose S. NURBS-based isogeometric analysis of buckling and free vibration problems for laminated composites plates with complicated cutouts using a new simple FSDT theory and level set method. Thin-Walled Structures 2016; 101: 141-156.

[39] Thai H-T, Vo TP, Bui TQ, Nguyen T-K. A quasi-3D hyperbolic shear deformation theory for functionally graded plates. Acta Mechanica 2014; 225: 951-964.

[40] Vu T-V, Nguyen N-H, Khosravifard A, Hematiyan MR, Tanaka S, Bui TQ. A simple FSDT-based meshfree method for analysis of functionally graded plates. Engineering Analysis with Boundary Elements 2017; 79: 1-12.

[41] Bui TQ, Nguyen MN, Zhang CZ. An efficient meshfree method for vibration analysis of laminated composite plates. Computational Mechanics 2011; 48: 175-193.

[42] Zhang LW. An element-free based IMLS-Ritz method for buckling analysis of nanocomposite plates of polygonal planform. Engineering Analysis with Boundary Elements 2017; 77: 10-25.

[43] Ansari R, Faghih Shojaei M, Gholami R. Size-dependent nonlinear mechanical behavior of third-order shear deformable functionally graded microbeams using the variational differential quadrature method. Composite Structures 2016; 136: 669-683.

[44] Yin SH, Hale JS, Yu TT, Bui TQ, Bordas SPA. Isogeometric locking-free plate element: A simple first order shear deformation theory for functionally graded plates. Composite Structures 2014; 118: 121-138.

[45] Yin SH, Yu TT, Bui TQ, Zheng XJ, Tanaka S. In-plane material inhomogeneity of functionally graded plates: A higher-order shear deformation plate isogeometric analysis. Composites Part B 2016; 106: 273-284.

[46] Liu S, Yu TT, Bui TQ, Yin SH, Thai DK, Tanaka S. Analysis of functionally graded plates by a simple locking-free quasi-3D hyperbolic plate isogeometric method. Composites Part B 2017;120: 182-196.

[47] Shen H-S. A two-step perturbation method in nonlinear analysis of beams, plates and shells. John Wiley & Sons Inc, 2013.

[48] Srinivas S, Rao AK. Buckling of thick rectangular plates. AIAA Journal 1969; 7(8): 1645-1646.

[49] Reddy JN, Phan ND. Stability and vibration of isotropic, orthotropic and laminated plates according to a higher-order shear deformation theory. Journal of Sound and Vibration 1985; 98(2): 157-170.

[50] Rao GV, Venkataramana J, Raju KK. Stability of moderately thick rectangular plates using a high precision triangular finite element. Computers & Structures 1975; 5(4): 257-259.

[51] Bhimaraddi A. Buckling and post-buckling behavior of laminated plates using the generalized nonlinear formulation. International Journal of Mechanical Sciences 1992; 34(9): 703-715.

[52] Xiang Y, Wang CM, Liew KM, Kitipornchai S. Mindlin plate buckling with prebuckling in-plane deformation. Journal of Engineering Mechanics ASCE 1993; 119(1): 1-18.

[53] Dym CL. Stability theory and its applications to structural mechanics. Noordhoff, Leyden, 1974.

[54] Yamaki N. Experiments on the postbuckling behavior of square plates loaded in edge compression. Journal of Applied Mechanics ASME 1961; 28: 238-244.

[55] Yasmin A, Daniel IM. Mechanical and thermal properties of graphite platelet/epoxy composites. Polymer 2004; 45(24): 8211-8219.

[56] Liu F, Ming P, Li J. Ab initio calculation of ideal strength and phonon instability of graphene under tension. Physical Review B 2007; 76(6): 064120.

Appendix A

The differential operators in Eqs. (25)-(28) are

$$L_{11} = \gamma_{110}\frac{\partial^2}{\partial x^2} + \gamma_{112}\frac{\partial^2}{\partial y^2}, \quad L_{12} = \gamma_{120}\frac{\partial}{\partial x}, \quad L_{13} = \gamma_{131}\frac{\partial}{\partial y},$$

$$L_{21} = \frac{\partial^4}{\partial x^4} + \gamma_{212}\frac{\partial^4}{\partial x^2\partial y^2} + \gamma_{214}\frac{\partial^4}{\partial y^4},$$

$$L_{31} = \gamma_{310}\frac{\partial}{\partial x}, \quad L_{32} = \frac{\partial^2}{\partial x^2} + \gamma_{322}\frac{\partial^2}{\partial y^2} + \gamma_{32}, \quad L_{33} = \gamma_{331}\frac{\partial^2}{\partial x\partial y},$$

$$L_{41} = \gamma_{411}\frac{\partial}{\partial y}, \quad L_{42} = \gamma_{421}\frac{\partial^2}{\partial x\partial y}, \quad L_{43} = \gamma_{430}\frac{\partial^2}{\partial x^2} + \gamma_{432}\frac{\partial^2}{\partial y^2} + \gamma_{43},$$

in which

$$[\gamma_{110}, \gamma_{112}] = k_S a^2 [K_{22}, \beta^2 K_{11}] / (\pi^2 D_{11}^*),$$

$$\gamma_{120} = k_S K_{22} a^2 / (\pi^2 D_{11}^*),$$

$$\gamma_{131} = k_S \beta K_{11} a^2 / (\pi^2 D_{11}^*)$$

$$[\gamma_{212}, \gamma_{214}] = \beta^2 [2A_{12}^* + A_{33}^*, \beta^2 A_{11}^*] / A_{22}^*$$

$$\gamma_{310} = -k_S K_{22} a^2 / (\pi^2 D_{11}^*),$$

$$[\gamma_{322}, \gamma_{32}] = [\pi^2 \beta^2 D_{33}^*, -k_S K_{22} a^2] / (\pi^2 D_{11}^*)$$

$$\gamma_{331} = \beta(D_{12}^* + D_{33}^*) / D_{11}^*,$$

$$\gamma_{411} = -k_S \beta a^2 K_{11} / (\pi^2 D_{11}^*),$$

$$\gamma_{421} = \beta \left(D_{12}^* + D_{33}^* \right) \Big/ D_{11}^*$$

$$\left[\gamma_{430}, \gamma_{432}, \gamma_{43} \right] = \left[\pi^2 D_{33}^*, \pi^2 \beta^2 D_{22}^*, -k_S K_{11} a^2 \right] \Big/ \pi^2 D_{11}^*$$

Appendix B

Excepting $b_{00}^{(k)}$ and $B_{00}^{(k)}$, coefficients shown in Eqs. (55)-(58) are

$$C_{11}^{(1)} = \frac{g_{11}^C}{g_{11}} A_{11}^{(1)}, \quad D_{11}^{(1)} = \frac{g_{11}^D}{g_{11}} A_{11}^{(1)},$$

$$B_{20}^{(2)} = \frac{\beta^2 n^2}{32 m^2} (2\mu + 1) A_{11}^{(1)2}, \quad B_{02}^{(2)} = \frac{\beta^2 m^2}{32 n^2 \gamma_{214}} (2\mu + 1) A_{11}^{(1)2},$$

$$A_{13}^{(3)} = \frac{g_{13}^A}{g_{13}} A_{11}^{(1)3}, \quad C_{13}^{(3)} = \frac{g_{13}^C}{g_{13}} A_{11}^{(1)3}, \quad D_{13}^{(3)} = \frac{g_{13}^D}{g_{13}} A_{11}^{(1)3},$$

$$A_{31}^{(3)} = \frac{g_{31}^A}{g_{31}} A_{11}^{(1)3}, \quad C_{31}^{(3)} = \frac{g_{31}^C}{g_{31}} A_{11}^{(1)3}, \quad D_{31}^{(3)} = \frac{g_{31}^D}{g_{31}} A_{11}^{(1)3},$$

$$B_{20}^{(4)} = -\frac{g_{31}^A}{g_{31}} \frac{\beta^2 n^2 (1+\mu)}{16 m^2} A_{11}^{(1)4}, \quad B_{02}^{(4)} = -\frac{g_{13}^A}{g_{13}} \frac{\beta^2 m^2 (1+\mu)}{16 \gamma_{214} n^2} A_{11}^{(1)4},$$

$$B_{22}^{(4)} = \frac{\beta^2 m^2 n^2 (1+\mu)}{4 \left(m^4 + \gamma_{212} m^2 n^2 + \gamma_{214} n^4 \right)} \left(\frac{g_{13}^A}{g_{13}} + \frac{g_{31}^A}{g_{31}} \right) A_{11}^{(1)4},$$

$$B_{42}^{(4)} = -\frac{\beta^2 m^2 n^2 (1+\mu)}{256 m^4 + 64 \gamma_{212} m^2 n^2 + 16 \gamma_{214} n^4} \frac{g_{31}^A}{g_{31}} A_{11}^{(1)4},$$

$$B_{24}^{(4)} = -\frac{\beta^2 m^2 n^2 (1+\mu)}{16 m^4 + 64 \gamma_{212} m^2 n^2 + 256 \gamma_{214} n^4} \frac{g_{13}^A}{g_{13}} A_{11}^{(1)4},$$

$$B_{40}^{(4)} = \frac{\beta^2 n^2 (1+\mu)}{64 m^2} \frac{g_{31}^A}{g_{31}} A_{11}^{(1)4}, \quad B_{04}^{(4)} = \frac{\beta^2 m^2 n^2 (1+\mu)}{64 \gamma_{214}} \frac{g_{13}^A}{g_{13}} A_{11}^{(1)4}$$

in which

$$g_{11}^C = \begin{vmatrix} m\gamma_{310} & mn\gamma_{331} \\ n\gamma_{411} & m^2\gamma_{430} + n^2\gamma_{432} - \gamma_{43} \end{vmatrix}, \quad g_{11}^D = \begin{vmatrix} m^2 + n^2\gamma_{322} - \gamma_{32} & m\gamma_{310} \\ mn\gamma_{421} & n\gamma_{411} \end{vmatrix},$$

$$g_{11} = \begin{vmatrix} m^2 + n^2\gamma_{322} - \gamma_{32} & mn\gamma_{331} \\ mn\gamma_{421} & m^2\gamma_{430} + n^2\gamma_{432} - \gamma_{43} \end{vmatrix},$$

$$g_{13}^A = \begin{vmatrix} (1+\mu)(2\mu+1)\dfrac{\beta^4 m^4}{16\gamma_{214}} & m\gamma_{120} & 3n\gamma_{131} \\ 0 & \gamma_{32} - m^2 - 9\gamma_{322}n^2 & -3mn\gamma_{331} \\ 0 & -3mn\gamma_{421} & \gamma_{43} - \gamma_{430}m^2 - 9\gamma_{432}n^2 \end{vmatrix},$$

$$g_{13}^C = \begin{vmatrix} m^2\gamma_{110} + 9n^2\gamma_{112} - m^2\beta^2 B_{00}^{(0)} - 9n^2\beta^2 b_{00}^{(0)} & (1+\mu)(2\mu+1)\dfrac{\beta^4 m^4}{16\gamma_{214}} & 3n\gamma_{131} \\ m\gamma_{310} & 0 & -3mn\gamma_{331} \\ 3n\gamma_{411} & 0 & \gamma_{43} - \gamma_{430}m^2 - 9\gamma_{432}n^2 \end{vmatrix}$$

$$g_{13}^D = \begin{vmatrix} m^2\gamma_{110} + 9n^2\gamma_{112} - m^2\beta^2 B_{00}^{(0)} - 9n^2\beta^2 b_{00}^{(0)} & m\gamma_{120} & (1+\mu)(2\mu+1)\dfrac{\beta^4 m^4}{16\gamma_{214}} \\ m\gamma_{310} & \gamma_{32} - m^2 - 9\gamma_{322}n^2 & 0 \\ 3n\gamma_{411} & -3mn\gamma_{421} & 0 \end{vmatrix}$$

$$g_{13} = \begin{vmatrix} m^2\gamma_{110} + 9n^2\gamma_{112} - m^2\beta^2 B_{00}^{(0)} - 9n^2\beta^2 b_{00}^{(0)} & m\gamma_{120} & 3n\gamma_{131} \\ m\gamma_{310} & \gamma_{32} - m^2 - 9\gamma_{322}n^2 & -3mn\gamma_{331} \\ 3n\gamma_{411} & -3mn\gamma_{421} & \gamma_{43} - \gamma_{430}m^2 - 9\gamma_{432}n^2 \end{vmatrix}$$

$$g_{31}^{A} = \begin{vmatrix} (1+\mu)(2\mu+1)\dfrac{\beta^4 n^4}{16} & 3m\gamma_{120} & n\gamma_{131} \\ 0 & \gamma_{32} - 9m^2 - \gamma_{322}n^2 & -3mn\gamma_{331} \\ 0 & -3mn\gamma_{421} & \gamma_{43} - 9\gamma_{430}m^2 - \gamma_{432}n^2 \end{vmatrix}$$

$$g_{31}^{C} = \begin{vmatrix} 9m^2\gamma_{110} + n^2\gamma_{112} - 9m^2\beta^2 B_{00}^{(0)} - n^2\beta^2 b_{00}^{(0)} & (1+\mu)(2\mu+1)\dfrac{\beta^4 n^4}{16} & n\gamma_{131} \\ 3m\gamma_{310} & 0 & -3mn\gamma_{331} \\ n\gamma_{411} & 0 & \gamma_{43} - 9\gamma_{430}m^2 - \gamma_{432}n^2 \end{vmatrix}$$

$$g_{31}^{D} = \begin{vmatrix} 9m^2\gamma_{110} + n^2\gamma_{112} - 9m^2\beta^2 B_{00}^{(0)} - n^2\beta^2 b_{00}^{(0)} & 3m\gamma_{120} & (1+\mu)(2\mu+1)\dfrac{\beta^4 n^4}{16} \\ 3m\gamma_{310} & \gamma_{32} - 9m^2 - \gamma_{322}n^2 & 0 \\ n\gamma_{411} & -3mn\gamma_{421} & 0 \end{vmatrix}$$

$$g_{31} = \begin{vmatrix} 9m^2\gamma_{110} + n^2\gamma_{112} - 9m^2\beta^2 B_{00}^{(0)} - n^2\beta^2 b_{00}^{(0)} & 3m\gamma_{120} & n\gamma_{131} \\ 3m\gamma_{310} & \gamma_{32} - 9m^2 - \gamma_{322}n^2 & -3mn\gamma_{331} \\ n\gamma_{411} & -3mn\gamma_{421} & \gamma_{43} - 9\gamma_{430}m^2 - \gamma_{432}n^2 \end{vmatrix}$$

Graphical Abstract